Materials Today Communications 52 (2026) 115019

Contents lists available at ScienceDirect

Materials Today Communications

journal homepage: www.elsevier.com/locate/mtcomm

Amorphous solid dispersions enhance the anticancer activity of quercetin in breast cancer

Davis Anu[a,1], K.P. Safna Hussan[a,b,c,d,*,1], Natália T. Correia[c], Florence Danède[c], G. Govindaraj[e], S. Lekshmi[f], Gowri Kalyani[f], Naoki Shinyashiki[b,g], Thekkekara D. Babu[a]

[a] *Amala Cancer Research Center (Recognized Research Centre, University of Calicut), Amalanagar, Thrissur - 680-555, Kerala, India*
[b] *Micro/Nano Technology Center, Tokai University, Hiratsuka-shi, Kanagawa 259-1292, Japan*
[c] *Univ. Lille, UMR 8207 - UMET - Unité Matériaux et Transformations, Lille F-59000, France*
[d] *Ayurgreen Scientifica Research Institute, Ayurgreen Campus, Kerala 679 582, India*
[e] *Department of Physics, School of Physical, Chemical and Applied Sciences, Pondicherry University, Puducherry 605 014, India*
[f] *Department of Physics, Sanatana Dharma College, Alapuzha, Kerala 688 003, India*
[g] *Department of Physics, School of Science, Tokai University, Hiratsuka-shi, Kanagawa 259-1292, Japan*

ARTICLE INFO

Keywords:
Breast cancer
Quercetin
Amorphous solid dispersions
Broadband dielectric spectroscopy

ABSTRACT

Rationale: Due to a broad spectrum of anticancer potential, quercetin (Qu) has attracted substantial attention. However, its biological application is hindered by poor water solubility and low bioavailability. Amorphous solid dispersion (ASD) technology has emerged as an effective formulation strategy to overcome these limitations by converting crystalline drugs into a high-energy amorphous state and improving molecular dispersion within suitable polymeric carriers.

Aim: To develop and characterise ASDs of Qu for enhanced anticancer properties.

Methods: ASDs of Qu were developed using PVP K30 at varying weight ratios, (Qu:PVP): ASD1 (1:9), ASD2 (1:4), and ASD3 (1:2.3). The amorphous nature, molecular interactions, thermal stability, and relaxation dynamics of ASDs were characterised using scanning electron microscope (SEM), differential scanning calorimetry (DSC), X-ray diffraction (XRD), fourier transform infrared spectroscopy (FTIR), thermal gravimetric analysis (TGA), and broadband dielectric spectroscopy (BDS). The biological efficacy of the optimized formulation is assessed through antiproliferative studies using breast cancer cell lines, MDA-MB-231 and MCF-7.

Results: SEM images showed the transformation of crystalline Qu into amorphous structures in the prepared ASDs, while Qu remained visible in the physical mixture. XRD showed amorphization of Qu in ASD1 and ASD2, identifying 1:9 and 1:4 ratios as optimal. However, ASD2 exhibited a mild tendency toward recrystallization. Pure Qu showed poor solubility (0.53 μM in water, 17.32 μM in ethanol), whereas ASDs significantly improved it (22.81–25.83 μM in water, 50.13–99.24 μM in ethanol). TGA showed Qu degradation at 375 K with major decomposition at 620 K (52% residue), whereas ASD1 degraded at 526.5 K and 820 K with 38.41% residue, indicating enhanced stability. DSC showed ASD1's glass transition at 395 K. BDS revealed a primary relaxation following VFT behaviour ($T_g \approx 438$ K, fragility index 116) and a secondary Arrhenius-type relaxation (activation energy 49.5 kJ/mol). ASD1 demonstrated significantly enhanced antioxidant and anti-inflammatory activities compared to pure quercetin in water. In the DPPH assay (2–10 μM), ASD1 in water showed 24% inhibition at 10 μM, compared with 3% for Qu in water, whereas Qu in DMSO reached 65%. In the superoxide scavenging assay (20–100 μM), ASD1 achieved 37% inhibition at 100 μM compared to 10% for Qu in water (58% in DMSO). Similarly, in the nitric oxide scavenging assay, ASD1 exhibited 28% inhibition at 100 μM, whereas Qu in water showed only 1.2% (51% in DMSO), confirming markedly improved bioactivity due to enhanced solubility and molecular dispersion. Cytotoxicity studies demonstrated that ASD1 exhibited lower IC_{50} values in ethanol against MDA-MB-231 (40.54 ± 0.55 μM vs 75.45 ± 3.4 μM for Qu) and MCF-7 (39.08 ± 0.55 μM vs 35.9 ± 1.28 μM for Qu), confirming its enhanced efficacy over pure quercetin.

Discussion: The results suggest that PVP K30-based ASDs enhance the physicochemical and biological properties of Qu. The increased solubility and thermal stability of ASD1 contributed to its superior antiproliferative activity

---

* Corresponding author at: Micro/Nano Technology Center, Tokai University, Hiratsuka-shi, Kanagawa 259-1292, Japan.
E-mail address: yfm4476@tokai.ac.jp (K.P.S. Hussan).

[1] These authors equally contribute to this work and share first authorship.

https://doi.org/10.1016/j.mtcomm.2026.115019
Received 10 October 2025; Received in revised form 15 March 2026; Accepted 18 March 2026

against TNBC cells. The intermediate fragility index observed by BDS supports its physical stability. Overall, ASD1, with the optimum drug-to-polymer ratio (1:9), shows strong potential as a formulation strategy to overcome Qu's biopharmaceutical limitations in cancer therapy.

Conclusion: The development of ASDs of Qu with PVP K30 significantly enhanced its solubility, thermal stability, and antiproliferative activity. These results support the potential of amorphous dispersion as a viable strategy to improve the therapeutic utility of poorly soluble anticancer compounds like Qu in breast cancer management.

1. Introduction

Quercetin (Qu), one of the most abundant plant-derived dietary flavonoids widely distributed in fruits and vegetables. Accumulating evidence suggests that quercetin is a promising functional food for the prevention and management of lifestyle-related diseases [1] including cancer [2]. Quercetin is cytotoxic to various cancer types, shows cell cycle arrest, and induces apoptosis [3] in various cancer cells including breast cancer [4]. Chemically, quercetin is 3,3′,4′,5,7-pentahydroxyflavone, a typical three-ring structure (A, B, and C rings) with five hydroxyl (OH) groups, which may undergo glycosylation to form various derivatives of quercetin [5–7]. *In vivo* studies shown that quercetin reduces tumours and improves survival in tumour-bearing mice [8] and reported to overcome multidrug resistance [9,10]. Co-treatment with quercetin significantly potentiated doxorubicin cytotoxicity in breast cancer cells by increasing intracellular drug accumulation and suppressing HIF-1α and P-glycoprotein expression [11].

Quercetin has been shown to suppress breast cancer stem cell proliferation, self-renewal, and invasiveness by downregulating key tumorigenic markers like ALDH1A1, CXCR4, MUC1, and EpCAM [12]. It induces apoptosis and inhibits proliferation in both ER-positive and triple-negative breast cancer cell models, including cells [13]. Mechanistically, quercetin modulates major oncogenic pathways, including Akt/mTOR/PTEN signalling [14], suppresses Twist-mediated survival pathways [15], and inhibits PKCδ/ERK/AP-1-dependent MMP-9 activation, thereby reducing tumour invasion and progression [16]. Beyond direct cytotoxicity, quercetin enhances antitumor immunity by promoting T-cell and NK-cell infiltration and inhibits myeloid-derived suppressor cells and tumour-associated macrophages [17]. Notably, the quercetin-derived microbial metabolite DOPAC has been reported to potentiate $CD8^+$ T-cell–mediated antitumor immunity *via* NRF2-dependent mitophagy [18]. *In vivo* studies also demonstrate reduced tumour progression and the mitigation of cancer-associated hepatic inflammation and fibrosis [19]. Collectively, these findings position quercetin as a promising multitargeted natural agent for breast cancer management.

However, its clinical translation remains limited by poor biopharmaceutical properties including high crystalline structure and strong intermolecular hydrogen bonding which make quercetin extremely poor aqueous solubility and bioavailability [20]. Studies using radiolabeled quercetin in rats have shown that only 20% of the administered dose is absorbed [21], and nearly 93% of quercetin undergoes metabolic conversion within one hour after oral administration at a dose of 10 mg/200 g body weight [22]. Quercetin undergoes extensive first-pass metabolism and is subject to active efflux by P-glycoprotein transporters in the intestinal epithelium, leading to very low oral bioavailability [23]. Because of its high permeability but low aqueous solubility, quercetin is classified as a BCS class II drug. Therefore, improving its solubility could make it an ideal candidate for drug development [24].

To address these limitations, multiple delivery approaches have been investigated. Nano-based systems including cyclodextrin inclusion complexes, polymeric nanoparticles, micelles, and solid lipid nanoparticles have shown improved dissolution and pharmacokinetics exposure of quercetin [25]. PEGylated liposomes have demonstrated enhanced solubility and greater cytotoxicity in cervical cancer models [26], while zein-based nanoparticles and β-lactoglobulin encapsulation systems have improved stability, bioaccessibility, and controlled release behaviour [26]. Additionally, pharmaceutical excipients and bioenhancers such as TPGS, sodium oleate, and piperine have been explored to inhibit efflux transporters and metabolic enzymes, thereby improving intestinal absorption. However, many of these nanoemulsion-based systems suffer from practical limitations, including high surfactant requirements, formulation complexity, potential long-term safety concerns, and relatively low drug-loading capacity issues.

Amorphous solid dispersion (ASD) technology has undergone substantial evolution since its introduction in the early 1960s, progressing from simple binary drug–polymer systems to sophisticated multicomponent architectures [33]. In ASD formulations, the API is stabilized in a high-energy amorphous state within a polymeric matrix, which markedly elevates the apparent solubility and dissolution rate relative to the corresponding crystalline form [34]. The clinical utility of ASDs is underscored by the approval of 48 drug products incorporating ASDs by the U.S. Food and Drug Administration between 2012 and 2023, spanning therapeutic areas including antiviral, antineoplastic, and metabolic indications. The most commonly employed polymeric carriers in approved ASD products are polyvinylpyrrolidone-vinyl acetate copolymer (PVPVA/copovidone, 49%) and hydroxypropyl methylcellulose acetate succinate (HPMCAS, 30%), prepared predominantly by spray drying or hot melt extrusion [35].

Recent structural advances in ASD design include: (i) ternary systems combining a drug, polymer, and surfactant (e.g., poloxamer 188, TPGS), which enhance supersaturation maintenance and reduce recrystallization risk under humid storage conditions [36,37]; (ii) cellulose-derivative carriers such as HPMCAS, carboxymethylcellulose acetate butyrate (CMCAB), 6-carboxycellulose acetate butyrate (CCAB), and cellulose acetate suberate (CASub), which offer pH-triggered release and superior crystallization inhibition via strong hydrogen bond interactions with the drug [38]; (iii) co-amorphous systems (CAMS) in which a drug is co-amorphized with a small-molecule co-former such as an amino acid, flavonoid, or organic acid, circumventing the limitations of polymeric carriers and often conferring synergistic biological activity [39,40]; and (iv) nanosized amorphous solid dispersions (NASDs) that combine amorphous state benefits with nanoparticle-mediated permeability enhancement [41]. Computational tools including machine learning, molecular dynamics simulations, and Flory–Huggins interaction parameters have further rationalized polymer–drug pairing and minimized trial-and-error in ASD development [42].

In the context of natural anticancer compounds, ASD technology has been applied with notable success to flavonoids including curcumin, naringenin, and quercetin (Qu), which share the limitation of extreme crystalline stability and poor aqueous solubility [43]. For quercetin specifically, PVP K30-based ASDs prepared by solvent evaporation at a 1:9 (Qu:PVP) weight ratio have demonstrated dissolution rates of approximately 95% within 120 min, compared to only ~19% for crystalline quercetin [44]. Studies employing HPMCAS, cellulose acetate butyrate blends, and PVP have further confirmed that the choice of carrier critically determines both the extent of crystallization inhibition and the release kinetics of quercetin, with PVP K30 offering the most favorable balance of wettability and supersaturation maintenance [38]. Building on this established framework, the present study aimed to develop and systematically characterize PVP K30-based ASDs of quercetin at varying drug-to-polymer ratios, and to evaluate the impact of amorphization on physicochemical stability and antiproliferative efficacy in breast cancer cell lines.

Therefore, there remained a compelling need for a simpler and scalable strategy to enhance the solubility and bioavailability of quercetin. In the present study, amorphous solid dispersions (ASDs) of Qu were developed by entrapping it within a polymer matrix of PVP K30, a biocompatible and biodegradable polymer, with the aim of enhancing its aqueous solubility and therapeutic efficacy. A key objective was to identify the optimum drug-to-polymer ratio that ensured a stable amorphous form of Qu without recrystallization. The formulations were characterized using differential scanning calorimetry (DSC), X-ray diffraction (XRD), fourier-transform infrared spectroscopy (FTIR), thermogravimetric analysis (TGA), and broadband dielectric spectroscopy (BDS) to confirm the amorphous nature, physical and thermal stability, molecular dynamics, glass transition phenomena, and molecular interactions between Qu and PVP. In addition, the antioxidant and anti-inflammatory potential of the optimized formulation were evaluated through *in vitro* DPPH radical scavenging, superoxide dismutase activity, and nitric oxide scavenging assays. The enhancement in biological activity was further assessed through *in vitro* antiproliferative studies against MCF-7 and MDA-MB-231 breast cancer cell lines using the MTT assay, to determine the therapeutic potential of the optimized ASD formulation.

2. Materials and methods

2.1. Chemicals

Quercetin hydrate (Qu) with a molecular weight (MW) of 302.24 g/mol was obtained from Tokyo Chemical Industry (Japan). PVP K30, with a MW of 30,000 g/mol, was sourced from Himedia (India). Ethanol and DMSO (MW 78.13 g/mol) were purchased from Merck (India). All chemicals used in this study were of analytical grade with a purity of 99.99% and were used without further purification.

2.2. Cell-lines

The human breast cancer cell lines, MCF-7 and MDA-MB-231, were obtained from the National Centre for Cell Science (NCCS), Pune, India. The cells were cultured in Dulbecco's Modified Eagle's Medium (DMEM; Gibco, Thermo Fisher Scientific, USA) supplemented with 10% heat-inactivated fetal bovine serum (FBS), streptomycin (100 μg/mL), and penicillin (100 U/mL). The cultures were maintained at 37 °C in a humidified incubator with 5% CO_2.

2.3. Preparation of ASDs

The amorphous ASD of Qu was prepared by entrapping it in polymer matrices of PVP-K30 in varying drug-to-polymer ratios (w/w; 1:9 (10:90), 1:4 (20:80), and 1:2.3 (30:70)). All ASDs were prepared using the solvent evaporation technique. Briefly, Qu and the PVP were weighed according to the predefined drug-to-polymer ratios for ASD1, ASD2, and ASD3, and then dissolved separately in 50 mL of ethanol in two beakers to prepare 1 g of ASD. The solutions were magnetically stirred at 60°C for 2 h to ensure complete dissolution of Qu and PVP, then the two solutions were mixed in a beaker, followed by further stirring at 70°C for an additional 2 h to obtain a clear and homogeneous solution. The solvent was then removed using a rotary evaporator, and the resulting residue was dried overnight in a hot-air vacuum oven to remove residual solvent. The dried solid dispersions were stored in airtight containers with silica gel until further analysis. The physical mixture (PM) was prepared by accurately weighing Qu and the polymer carrier in a 1:1 (w/w) ratio, then blending them thoroughly in a mortar and pestle at 303 K to obtain a uniform mixture. The prepared PM was stored in an airtight container until further characterization.

2.4. Scanning electron microscopy

The surface morphology of quercetin (Qu), the polymer (PVP), and the prepared amorphous solid dispersions (ASDs) was examined using a field emission scanning electron microscope (FE-SEM) (Hitachi S-4800 Field Emission Scanning Electron Microscope). The samples were mounted on aluminum stubs using double-sided conductive carbon tape and sputter-coated with a thin layer of platinum to improve electrical conductivity and minimize surface charging during analysis. The observations were performed under high vacuum at an accelerating voltage of 3.0 kV with a working distance of approximately 8 mm. Micrographs were obtained at a magnification of 17,000 ×, with a scale bar of 2 μm, to evaluate the surface morphology and structural characteristics of the samples.

2.5. X-ray diffraction

X-ray diffraction patterns of the samples Qu, PM and three formulated ASDs (ASD1, ASD2 and ASD3) were taken in a RIGAKU X-ray diffractometer with a Ni filter and with a rotating anode and CuKα radiation (1.5406 Å) from 10 to 80 (2θ angle).

2.6. Fourier transform infrared spectroscopy (FTIR)

FTIR spectra of the samples Qu, PM and three formulated ASDs (ASD1, ASD2 and ASD3) were recorded using KBr disc as in range 3500–400 cm^{-1} of JASCO FTIR-4100 spectrophotometer.

2.7. Thermogravimetry

The temperature-dependent behavior of Qu and the prepared ASD1 was investigated using thermogravimetric analysis (TGA) on the Q500 apparatus from TA Instruments. The analysis was conducted under a nitrogen gas (99.999%) atmosphere at a 50 mL/min constant flow rate. The experimental setup included alumina pans, and the heating rate was set at 10 K/min, with a temperature range from 283 K to 873 K [45,46].

2.8. Differential scanning calorimetry

The phase transitions of the ASD1 formulation were analyzed using Temperature-Modulated Differential Scanning Calorimetry (TMDSC) on a DSC Q2000 (TA Instruments) equipped with a refrigerated cooling system. The sample was placed in an aluminium crucible pan with a hole in its lid. The instrument was calibrated for both temperature and enthalpy using indium standards. The glass transition temperatures were determined at the onset of the corresponding [45,46].

2.9. Broadband dielectric spectroscopy

The dielectric measurements of ASD1 were carried out using Novocontrol GMBH Alpha dielectric spectrometer, in a wide frequency range from 10^{-1}Hz to 10^{7} Hz from deep glassy state to 473 K. The temperature was controlled by a Novocontrol Quatro Cryosystem temperature controller with temperature stability better than 0.1 K. Dielectric measurements were recorded on heating immediately after quench cooling a parallel plate cell made of stainless steel. The diameter was measured using screw gauge and silica spacers were used in between the samples to maintain gap between electrodes [45,47,48].

2.10. Solubility study

Solubility studies were conducted to assess the enhancement of Qu's solubility in the prepared ASDs. A calibration curve for Qu was first established using DMSO by preparing a 50 mM stock solution and measuring absorbance at 355 nm. Subsequently, solutions of Qu and their ASDs were prepared in a 1 mg/mL concentration using water and ethanol. After equilibration, the samples were filtered through a 0.4 µm hydrophilic membrane filter to remove undissolved particles, and the absorbance of the filtrates was measured at room temperature 298 K. The concentration of dissolved Qu was subsequently calculated using a previously established calibration curve.

2.11. *Antioxidant assays*

2.11.1. *DPPH radical scavenging assay*

The free radical scavenging activity of Qu, ASD1 formulation, and Qu in DMSO was evaluated using the DPPH (2,2-diphenyl-1-picrylhydrazyl) assay. A freshly prepared 0.1 mM DPPH solution was prepared in methanol and stock solutions of Qu in water, ASD1 in water, and Qu in DMSO were prepared and appropriately diluted to obtain final concentrations ranging from 2 to 10 µM. Briefly, varying volumes of the sample solutions (2–10 µL) were adjusted to a final volume of 1 mL of freshly prepared 0.1 mM DPPH solution. The reaction mixtures were vortexed gently and incubated in the dark at room temperature for 20 min to prevent photo-degradation of DPPH. After incubation, the absorbance was measured at 517 nm using a UV–Visible spectrophotometer. The percentage of DPPH radical scavenging activity was calculated using the following equation:

$$\% \quad Inhibition \quad = \frac{Abs_{control} - Abs_{sample}}{Abs_{control}} \times 100$$

Where $Abs_{control}$ is the absorbance of the DPPH solution without sample, Abs_{sample} is the absorbance in the presence of test sample. All experiments were performed in triplicate ($n = 3$), and results were expressed as mean ± SEM [49,50].

2.11.2. *Superoxide radical scavenging (SO) activity assay*

SO activity was determined based on the inhibition of nitro blue tetrazolium (NBT) reduction by superoxide radicals generated in a riboflavin–light system. The reaction mixture (final volume 3.0 mL) consisted of 50 mM phosphate buffer (pH 7.8), 75 µM NBT, 0.1 mM EDTA, and an appropriate volume of the sample. The reaction was initiated by the addition of 2 µM riboflavin and the tubes were exposed to incandescent light (15–20 W) for 15 min to induce superoxide radical formation. A control containing all reagents except the sample was prepared simultaneously, along with a non-illuminated blank for background correction. The reduction of NBT to blue formazan was measured spectrophotometrically at 560 nm. SO activity was expressed as percentage inhibition of NBT reduction using the formula:

$$\% \quad Inhibition \quad = \frac{Abs_{control} - Abs_{sample}}{Abs_{control}} \times 100$$

where $Abs_{control}$ represents the absorbance of the illuminated control and Abs_{sample} represents the absorbance in the presence of the test sample. One unit of SOD activity was defined as the amount of enzyme required to produce 50% inhibition under the assay conditions. All experiments were performed in triplicate ($n = 3$), and results were expressed as mean ±SEM.

2.12. *Anti-inflammatory assays*

The anti-inflammatory activity of the samples was evaluated by measuring nitric oxide (NO) scavenging activity using the sodium nitroprusside–Griess reagent method. Sodium nitroprusside in aqueous solution at physiological pH spontaneously generates nitric oxide, which reacts with oxygen to form nitrite ions. These nitrite ions were quantified using Griess reagent. Briefly, 2 mL of 10 mM sodium nitroprusside prepared in phosphate-buffered saline (PBS, pH 7.4) was mixed with different concentrations of the test samples. The reaction mixture was incubated at room temperature under light for 2 h. After incubation, 0.5 mL of the reaction mixture was mixed with 0.5 mL of Griess reagent (composed of 1% sulfanilamide, 0.1% N-(1-naphthyl) ethylenediamine dihydrochloride, and 2% phosphoric acid). The mixture was allowed to stand for 10 min at room temperature for color development. The absorbance of the resulting chromophore was measured at 540 nm using a UV–Visible spectrophotometer. A control containing sodium nitroprusside without sample was prepared simultaneously.

The percentage inhibition of nitric oxide production was calculated using the following formula:

$$\% \quad Inhibition \quad = \frac{Abs_{control} - Abs_{sample}}{Abs_{control}} \times 100$$

where $Abs_{control}$ represents the absorbance of the control reaction and Abs_{sample} represents the absorbance in the presence of the test sample.

All experiments were performed in triplicate ($n = 3$), and results were expressed as mean ± standard deviation (SD) [51,52].

2.13. *Cytotoxicity analysis*

The 5000 cells per well of, MCF-7 and MDA-MB-231 were seeded with 100 µL of DMEM medium in each well of a 96-well plate. After 24 h, the medium was replaced, and the cells were treated with varying concentrations of Qu and ASD1 in different solvents at 37°C for 3 days. A blank, containing complete culture medium without cells, was also maintained. After incubation, photographs were taken using an inverted microscope (Carl ZEISS, Oberkochen, Germany) equipped with a binocular phototube and an integrated HD camera (Primovert HDcam, 5 MP). Subsequently, 100 µL of 3-(4,5-dimethylthiazol-2-yl)-2,5-diphenyltetrazolium bromide (MTT) solution was added to each well and incubated for 4 h. The resulting formazan crystals were then dissolved by replacing the medium in each well with 100 µL of DMSO. The absorbance of the formazan-dissolved solution was measured at 570 nm using a microplate reader (BioTek, USA) [50–54].

The biocompatibility of the PVP polymer was evaluated using an in vitro cytotoxicity assay with HEK-293 cells. Cell morphology under control conditions and after treatment with Lpm (10 µM) and PVP polymer (100 µM) was examined microscopically. Representative images are provided in Supplementary Figure S8.

2.14. *Statistical analysis*

All *in vitro* experimental data are presented as mean ± standard error of the mean (SEM) from at least three independent experiments ($n = 3$). Statistical significance was determined using a One-Way Analysis of Variance (ANOVA) to compare the means across different concentration groups. To identify specific differences between each experimental treatment (Qu in ethanol, Qu in DMSO, ASD1 in water, and ASD1 in ethanol) and the control group (Qu in water), a Dunnett's post-hoc test was performed. This test was chosen specifically to compare multiple treatment arms against a single reference control. The threshold for statistical significance was set at $p < 0.05$. In the figures, degrees of significance are indicated as follows: $p < 0.05$ (*), $p < 0.01$ (**), $p < 0.001$ (***), $p > 0.05$, was considered not significant (ns).

3. Results and discussion

3.1. *Morphology*

Fig. 1 illustrates the SEM images of Qu, PM, and prepared ASDs. Pure Qu (Fig. 1.a) exhibits a well-defined needle-shaped crystalline morphology with smooth surfaces and sharp edges, indicating its highly crystalline nature. These elongated crystals confirm the highly crystalline nature of quercetin, which is consistent with its poor aqueous solubility. The presence of regular crystal facets indicates a well-ordered

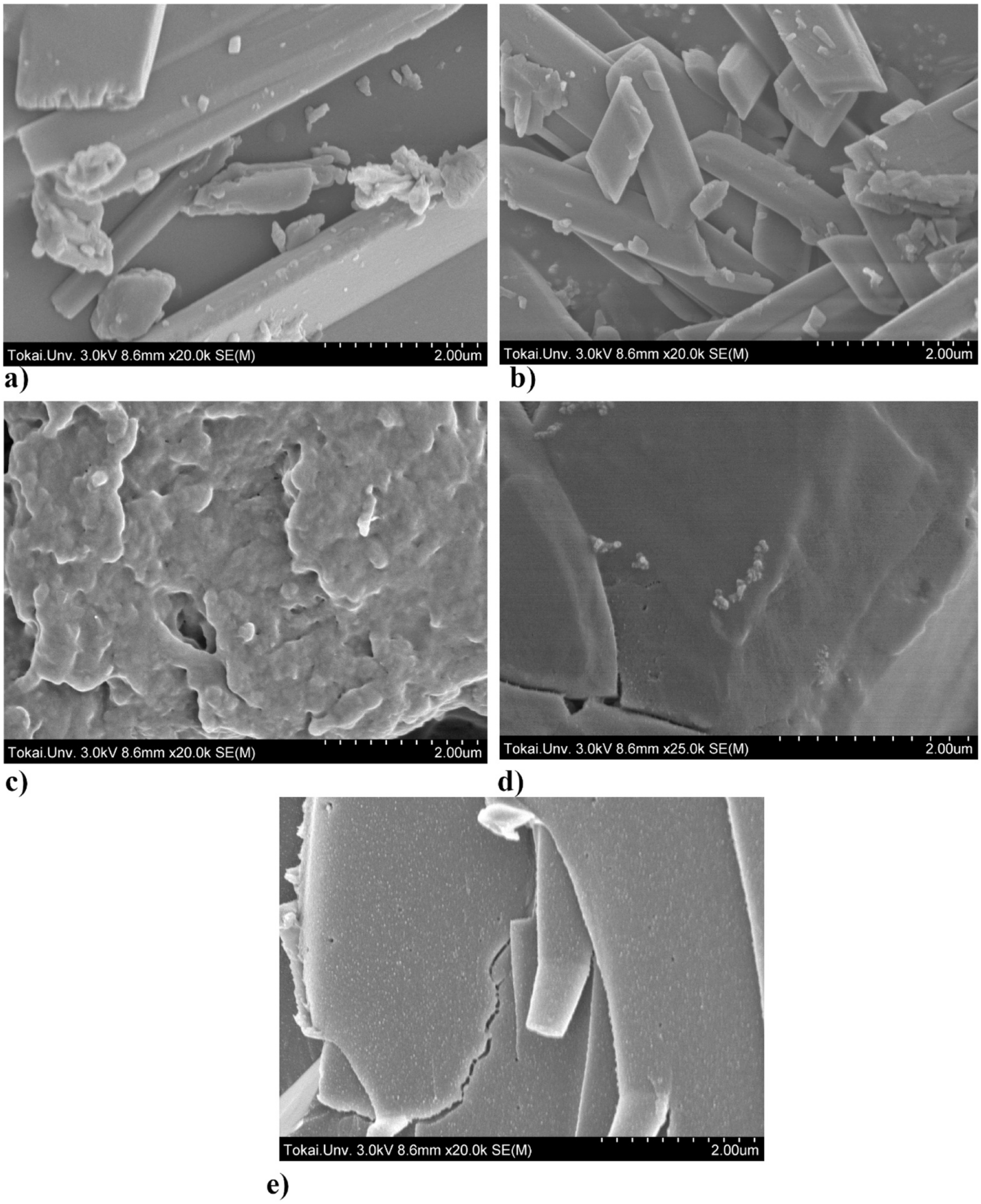

Fig. 1. SEM micrographs of (a) Qu, (b) PM, (c) ASD1, (d) ASD2, and (e) ASD3 obtained at 17,000 × magnification (scale bar = 2 μm).

molecular arrangement. In the physical mixture (Fig. 1.b), the crystalline quercetin particles can still be distinguished from the polymer flakes, indicating that no structural transformation has occurred. In ASD1 (Fig. 1.c), the original needle-shaped crystals of quercetin are no longer clearly visible. Instead, the particles appear as irregular, aggregated flakes with rough surfaces, suggesting that quercetin has been partially dispersed within the polymer matrix. ASD2 (Fig. 1.d) shows a more homogeneous and smooth flake-like morphology with almost complete disappearance of crystalline quercetin structures. The absence of sharp crystal edges suggests successful molecular dispersion of quercetin in the PVP matrix, indicating a higher degree of amorphization compared to ASD1. In ASD3 (Fig. 1.e), some plate-like crystalline fragments reappear along with the polymer matrix, suggesting partial recrystallization or incomplete dispersion of quercetin. Compared with ASD2, the presence of these crystalline features indicates lower amorphous stability.

3.2. *Amorphization and optimal drug loading in ASDs*

The XRD patterns of PVP, Qu, PM, ASD1, ASD2, and ASD3 are presented in Fig. 2. Pure PVP exhibited a typical amorphous diffraction pattern characterized by broad diffuse halos centered around $2\theta \approx 10^\circ$ and 20°, confirming the absence of long-range crystalline order in the polymer matrix. In contrast, pristine Qu showed a highly crystalline nature with sharp diffraction peaks at 2θ values of 10.75°, 12.47°, and 27.43°, in good agreement with previously reported data [55]. These characteristic crystalline peaks were also clearly observed in the physical mixture (PM), indicating that simple blending did not alter the crystalline structure of Qu.

Notably, the diffraction patterns of ASD1 and ASD2 were dominated by the amorphous halos of PVP, while the characteristic crystalline peaks of Qu completely disappeared, suggesting successful amorphization and homogeneous molecular dispersion of Qu within the PVP K30 matrix. However, in ASD3, a weak diffraction peak reappeared at 2θ

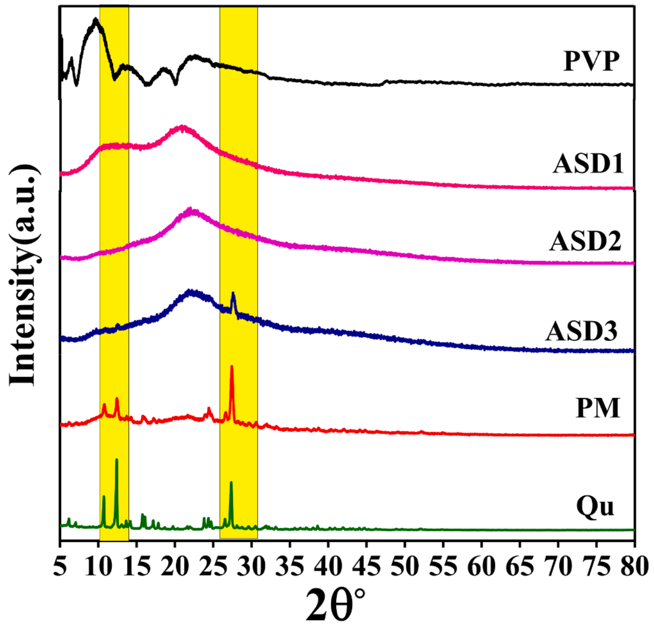

Fig. 2. X-ray diffraction patterns of pure Qu; PM; solid dispersions ASD1, ASD2, ASD3.

= 27.43°, indicating partial recrystallization of Qu at higher drug loading. Therefore, the XRD results demonstrate that ASD1 and ASD2 provide optimal drug loading conditions, where Qu remains in a fully amorphous state, which is expected to improve physical stability and enhance potential bioavailability.

3.3. FTIR

The interactions between PVP K30 and Qu in the solid dispersion systems were examined using FTIR analysis, spanning a wavelength range from 4000 to 500 cm^{-1} (Fig. 3) and the characteristic peaks were tabulated in Tables 1 and 2. Pure Qu exhibited a broad absorption band around 3485 cm^{-1} corresponding to O–H stretching vibrations. The characteristic carbonyl (C=O) stretching vibration appeared at approximately 1732 cm^{-1} , while aromatic C=C stretching vibrations were observed in the region of 1658 cm^{-1} and C-H bending at 1464 cm^{-1} . Additional bands in the range of 1284 cm^{-1} were attributed to C–O stretching and phenolic bending vibrations by aromatic ring deformation at 735 cm^{-1}, aromatic deformation at 649 cm^{-1}, skeletal vibration at 576 cm^{-1} and ring deformation at 521 cm^{-1} confirming the chemical integrity of Qu [56].

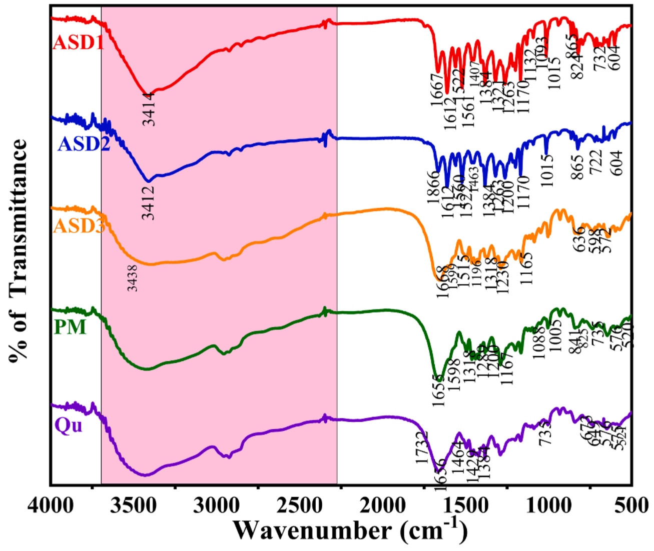

Fig. 3. FTIR spectra of pure Qu; PM; solid dispersions ASD1, ASD2, ASD3.

Table 1
Summary of the mechanism of action of Qu against TNBC.

Mechanism	Description	Key Pathways	Ref
Apoptosis induction	Promotes programmed cell death	↑ Caspase −3, Caspase-9, ↓ Bcl-2	[27]
Inhibition of cell proliferation	Halts cell cycle progression and suppresses growth	↓ Cyclins, CDKs; G1 or G2/M arrest	[28]
Signalling pathway modulation	Disrupts pro-survival and proliferative signalling pathways	↓PI3K/Akt/ mTOR, MAPK/ ERK, NF-kB	[29]
Anti-metastatic activity	Reduces migration and invasion by affecting extracellular matrix remodelling and EMT	↓ MMP-2.MMP-9; ↓ Vimentin, N-cadherin	[30]
Antioxidant / anti-inflammatory	Neutralises oxidative stress and inflammation, contributing to tumour regression	↓ROS, COX-2, iNOS	[31]
Cancer stem cell inhibition	Targets and depletes TNBC cancer stem cell population	↓ Notch, Wnt/ β-catenin pathways	[32]

Table 2
Comparison of characteristic FTIR absorption bands of Qu, PM, and ASDs (ASD1, ASD2, ASD3).

Qu (cm^{-1})	PM (cm^{-1})	ASD1 (cm^{-1})	ASD2 (cm^{-1})	ASD3 (cm^{-1})	Assignment
3485	3458	—	—	—	O–H stretching (free hydroxyl)
3434	3430	3414	3412	3436	H-bonded O–H stretching
1732	—	1667	1866	1668	C=O stretching
1658	1655	1612	1612	1599	Aromatic C=C stretching
1464	1598	1522	1522	1515	C–H bending
1429	—	1407		—	Aromatic ring vibration
1384	—	1384	1384	1396	Phenolic O–H bending
1284	1289		1263	—	C–O stretching
—					C–O stretching (polymer + Qu overlap)
—	1318	1321		1318	C–O stretching (polymer + Qu overlap)
—	—	—		1230	C–O–C stretching
—	1200	1170	1170	1165	Ether linkage stretching
—	1088	1093	—	—	Polymer backbone vibration
—	1005	1015	1015	1015	C–O stretching
735	735	733	722	—	Aromatic ring deformation
673	—	—	—	—	Out-of-plane bending
649	—	636	604	636	Aromatic deformation
576	576	572	—	598 / 572	Skeletal vibration
521	520	—	—	—	Ring deformation mode

The PM displayed a superposition of characteristic peaks from both Qu and the polymer carrier, with no significant peak shifts or intensity changes. Almost all peaks of Qu at 3458, 3430, 1655, 1598, 1289, 735, 576 and 520 cm^{-1} were retained in the PM. In addition, C-O stretching was observed at 1318 cm^{-1} from the PVP-Qu overlap. In contrast, all ASDs (ASD1, ASD2, ASD3) exhibited noticeable spectral modifications. Aromatic C=C stretching vibrations of Qu at 1658 cm^{-1} were retained in PM at 1655 cm^{-1} , confirming the absence of structural alteration during physical mixing. In contrast, these bands shifted to lower wavenumbers in ASD formulations (1612 cm^{-1} in ASD1 and ASD2, and 1599 cm^{-1} in ASD3), indicating reduced crystallinity and enhanced molecular disorder. Similarly, the C–H bending vibration at 1464 cm^{-1} in pure Qu shifted to 1522 cm^{-1} in ASD1 and ASD2 and 1515 cm^{-1} in ASD3, reflecting changes in the molecular environment due to polymer–drug interactions. The aromatic ring vibration band of Qu at 1429 cm^{-1} was either reduced or disappeared in ASD samples, while the phenolic O–H bending vibration at 1384 cm^{-1} was retained with minor shifts (1384–1396 cm^{-1}) in solid dispersions. These changes further indicate partial disruption of Qu's crystalline lattice without chemical degradation. The C–O stretching vibration of Qu at 1284 cm^{-1} showed slight shifting and peak suppression in ASD formulations (1263 cm^{-1} in ASD2), suggesting interaction of oxygen-containing functional groups with the polymer carrier.

In the fingerprint region, polymer-related overlapping bands appeared at 1318–1321 cm^{-1} , confirming the coexistence of polymer and Qu within the solid dispersion matrix. Ether linkage stretching vibrations observed at 1200 cm^{-1} in PM shifted to 1170 cm^{-1} in ASD1 and ASD2 and 1165 cm^{-1} in ASD3, indicating conformational changes in the polymer network induced by drug incorporation. Additional C–O stretching vibrations at 1005–1015 cm^{-1} were retained in all ASD formulations, suggesting the chemical stability of Qu.

The low-frequency region (800–500 cm^{-1}), associated with aromatic ring deformation and skeletal vibrations, also showed noticeable changes. The aromatic ring deformation peak at 735 cm^{-1} shifted slightly to 733 cm^{-1} in ASD1 and 722 cm^{-1} in ASD2, while skeletal vibrations at 576 cm^{-1} shifted to 572–598 cm^{-1} in ASDs. The disappearance or broadening of several low-frequency peaks in solid dispersions further confirms loss of long-range crystalline order and formation of an amorphous phase [29].

3.4. Enhanced Qu solubility

Studies suggest that Qu exhibits an amphipathic behaviour because of the hydroxyl groups that make up the polar portion and the phenyl rings that form the hydrophobic part of the molecules [57]. These compounds have variable properties depending on the charge density of their hydrophilic and hydrophobic components, including their aqueous solubility and resulting antioxidant capacity. The solubility of Qu depends on the temperature, pH [58] and nature of the solvent, also structural features, and thermodynamic properties of the compound [59] etc., Qu's aqueous solubility at 20°C has been reported to be less than 0.01 g/L [60]; however, precise solubility measurements remain limited in the literature. Up to 80°C, the aqueous solubility of Qu dihydrate was comparable to that of anhydrous Qu. The solubility of Qu dihydrate in water was 1.5–2.5 times greater than that of Qu anhydrous at temperatures exceeding or equal to 100 °C

In this study, the solubility of pure Qu in water and ethanol was 0.53 and 17.32 μM. The solubility of ASDs in the ratio (ASD1, ASD2, and ASD3) was 25.83, 22.62, and 22.81 μM in water and 50.13, 69.67, and 99.24 μM in ethanol, respectively. All of the formulations showed an increase in drug solubility in ethanol compared to pure Qu. The enhanced absorbance of ASDs, particularly in ethanol, demonstrates improved solubility and dispersion of Qu compared to its native form in water, as illustrated in Fig. 4 and summarised in Table 3.

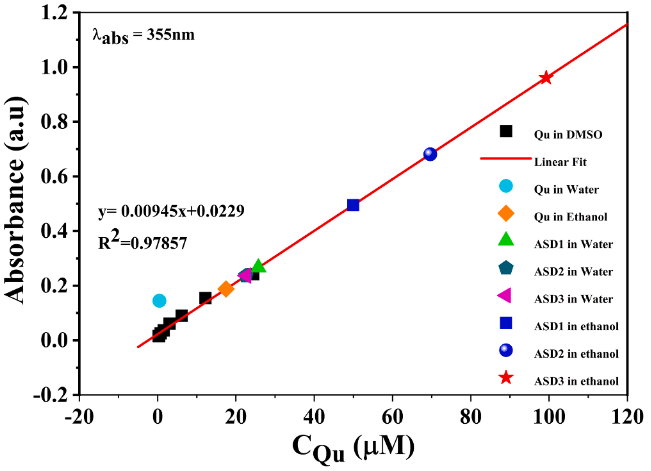

Fig. 4. Calibration curve showing the linear relationship between absorbance at 355 nm and Qu and ASD's concentration in various solvents: water, ethanol and DMSO. Qu in DMSO (black squares) was used to establish the standard curve ($y = 0.00945x + 0.0229$, $R^2 = 0.97857$).

Table 3
Concentration of Qu dissolved and corresponding absorbance values for pure Qu and prepared ASDs at various ratios ASD1 (1:9), ASD2 (2:8), and ASD3 (3:7) in water and ethanol. Measurements were recorded at λ= 355 nm.

S. No.	Drug	Concentration of Qu (μM)	Absorbance
1	Qu in Water	00.53	0.145
2	Qu in Ethanol	17.32	0.188
3	ASD1 in Water	25.83	0.266
4	ASD1 in Ethanol	50.13	0.495
5	ASD2 in Water	22.62	0.236
6	ASD2 in Ethanol	69.67	0.681
7	ASD3 in Water	22.81	0.237
8	ASD3 in Ethanol	99.24	0.961

3.5. Thermal gravimetric properties

Based on the combined evaluation of XRD and solubility studies, ASD1 was selected as the optimized formulation for further detailed thermal and physicochemical characterization. ASD1 exhibited complete suppression of Qu crystalline peaks without any indication of recrystallization, along with a significant enhancement in aqueous solubility, which is critical for improving oral bioavailability. In contrast, ASD3 showed partial recrystallization behavior (exhibited the reappearance of a characteristic crystalline peak at $2\theta = 27.43$), while higher drug-loading formulations also pose increased risks of physical instability. In addition, solubility studies revealed that ASD1 provided a substantial improvement in Qu solubility compared to pure Qu and the physical mixture, particularly in aqueous medium, which is critical for oral bioavailability. While ASD2 and ASD3 showed higher solubility in ethanol, the aqueous solubility enhancement achieved by ASD1 was considered more relevant for pharmaceutical application and formulation performance. Considering these factors, as well as the high cost and experimental complexity associated with advanced thermal analyses, subsequent investigations were focused primarily on ASD1.

3.5.1. Thermogravimetric (TGA) Analysis

There have been reports of three distinct polymorphs of quercetin hydrates showing melting at 317, 318, and 323 °C and mass losses of endo-crystalline solvent (water) at 82, 105, and 119 °C. There have been reports of decomposition occurring at temperatures between 340 and 350 °C, which is marginally higher than the melting temperature [57]. Many comparable melting point values have been reported in other quercetin studies, such as 315°C with a heat of fusion of 51.08 kJ/mol and a glass transition at 108°C [58], 322°C with a heat of fusion of 41.5 kJ/mol [59], and, most recently, 323°C [60].

From the TGA graph in Fig. 5, the dashed line (representing Qu) shows this initial loss beginning around 375 K (≈102°C), stabilizing near 410 K (≈137°C). This aligns with the literature, which cites endothermic peaks and water loss in this temperature range. A second decomposition event occurs around 620 K (≈347°C), with approximately 52% of the material remaining, which matches previous reports of thermal degradation near 340–350°C. In contrast, the ASD1 formulation shows a clear rightward shift in the TGA curve (solid line). No

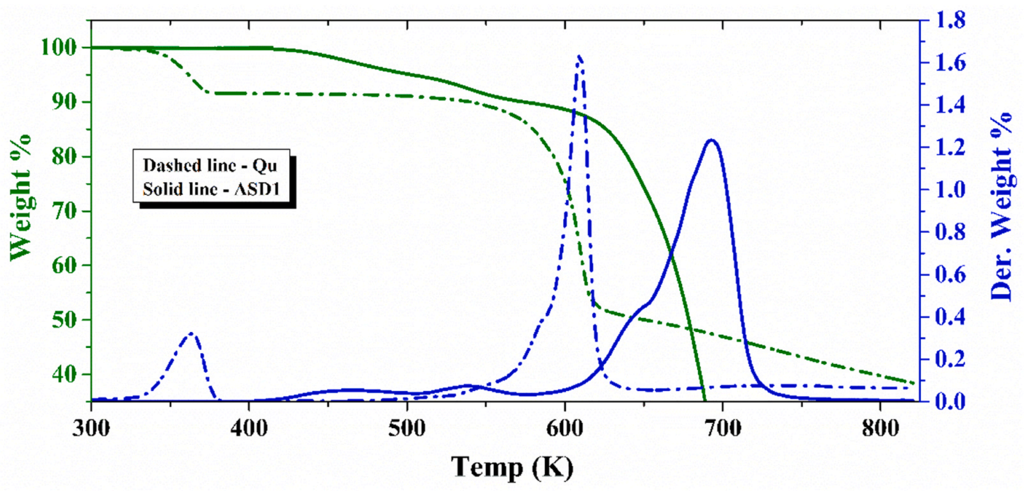

Fig. 5. Thermogravimetric (TGA) and derivative thermogravimetric (DTG) curves of Qu dihydrate (dashed line) and ASD1 formulation (solid line).

initial mass loss is observed in the 300–400 K range, confirming the absence of water. The first significant weight loss occurs at 253.38°C (≈526.5 K), resulting in a 9.51% loss. The major decomposition step occurs at 547.84°C (≈820 K), with 38.41% residue. This indicates improved thermal stability in ASD1 compared to pure Qu, likely due to reduced moisture and increased matrix protection.

3.5.2. *Differential scanning calorimetry*

Notably, since the degradation temperature is close to the melting point of Qu, quench cooling was avoided in order to trace the glass transition temperature Tg of Qu accurately; only ASD1 will be focused on from here onwards. The DSC thermogram of ASD1 exhibits a distinct glass transition temperature (T_g) at 395 K, as indicated by a step change in both the total heat flow (black curve) and the reversible heat flow (blue curve) in Fig. 6. The presence of a single, well-defined T_g suggests the formation of a homogeneous amorphous phase without any evidence of phase separation. The absence of sharp endothermic or exothermic peaks further confirms the lack of crystallinity, indicating complete amorphization of the formulation. The reversible heat flow profile, derived from modulated DSC, isolates the T_g as a purely thermodynamic event, removing kinetic contributions and reinforcing the thermal stability of the ASDs.

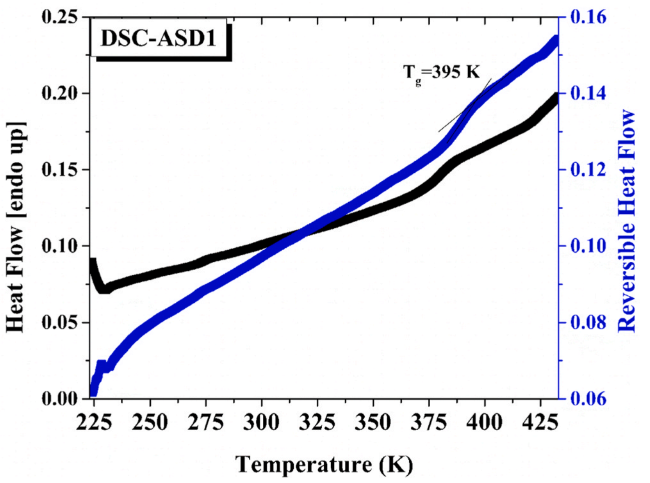

Fig. 6. DSC curve of Qu, total heat flow black line and reversible heat flow in blue line from TMDSC, obtained during heat at 5 °C/min.

3.6. *Molecular dynamics*

The dielectric behaviour of ASD1 was monitored using BDS across 19 temperatures from 293 to 473 K in steps of 10 K, over a wide frequency range from 10^{-1} Hz to 10^{7} Hz, to elucidate the macroscopic behaviour of ASD. Fig. 7 depicts the temperature dependent behaviour of dielectric loss during the quench cooling after heating scan to 473 K the sample and to remove water /moisture for selected frequencies (isochronal plots at 1.89 Hz, 9.69 Hz, 4.96 $\times 10^{3}$ Hz and 2.54 $\times 10^{5}$ Hz). Two relaxations processes are observed, one process with high dielectric strength emerging around 400 K and a weak broad process in the lower temperature region over 300–400 K.

The spectral induced polarization loss current is manifested by frequency-dependent behaviour of dielectric loss. This phenomenon is also called the 'low-frequency dielectric dispersion and absorption' of the electrical conductivity (or its inverse, the electrical resistivity). So far, no unique physical–chemical model has been developed to describe the frequency dispersion; therefore, the most used approach is to fit the experimental data based on phenomenological models.

This dielectric behaviour at 19 temperatures is modelled by a series of modified Cole-Cole type equations, one of the commonly used phenomenological models with a term that accounts for the contribution of electrode effect (EE) (Figure S5, S6 and S7 in supplementary material) at higher temperatures [61]. For the temperatures in the range (1): T = 433, 443, 453, two Cole-Cole dielectric function for intrinsic dielectric processes with intrinsic bulk resistivity ρ_b and non-intrinsic Cole-Cole type of electrode (E) polarization is identified as:

$$\begin{aligned}\epsilon^{*}(\omega) &= \frac{1}{M^{*}(\omega)} = \frac{1}{i\omega C_0 Z^{*}(\omega)} = \frac{1}{i\omega\epsilon_0\rho^{*}(\omega)} = \frac{\sigma^{*}(\omega)}{i\omega\epsilon_0}\\ &= \frac{1}{i\omega\epsilon_0}(\rho_b + E)^{-1} + \epsilon_\infty + d_1 + d_2, \end{aligned} \tag{1}$$

where $\varepsilon^*(\omega) = \varepsilon'(\omega) - i\varepsilon''(\omega)$ is the complex permittivity, $Z^*(\omega)$ is the complex impedance, $C_0 = \varepsilon_0 A/d$ is the geometric capacitance of the empty sample cell, with ε_o as vacuum permittivity, A is electrode area, and d as sample thickness, $\sigma^*(\omega)$ is the complex conductivity, ε_0 is the vacuum permittivity ($\approx 8.854 \times 10^{-12}$ F/m), ε_∞ is the high-frequency limit of permittivity, $M^*(\omega) = \frac{1}{\varepsilon^*(\omega)}$ is the complex electric modulus [62].

$$d_1 = \frac{\Delta\varepsilon_{!}}{1 + (i\omega\tau_1)^{\alpha_1}}, \quad \tau_1 = R_1 C_1$$

$$d_2 = \frac{\Delta\varepsilon_2}{1 + (i\omega\tau_2)^{\alpha_2}},\ E = \frac{\rho_e}{1 + (i\omega\tau_e)^{\alpha_e}},\ \tau_e = R_e C_e,\ \tau_2 = R_2 C_2,\ \omega = 2\pi f.$$

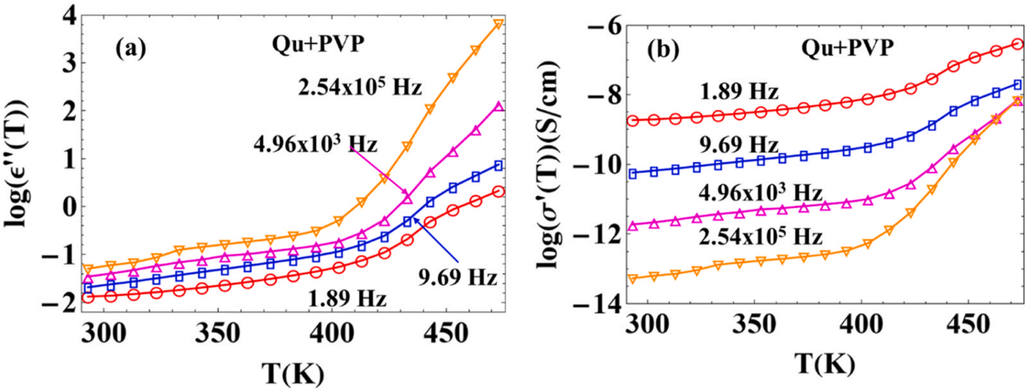

Fig. 7. Temperature dependent a) dielectric loss and b) conductivity spectra against temperature at four selected frequencies; 1.89 Hz (red circles), 9.69 Hz (blue squares), 4.96 × 10^3 Hz (magenta up triangles) and 2.54 × 10^5 Hz (orange down triangles) for ASD1 (10:90; Qu:PVP); data taken from isothermal measurements.

$\Delta\epsilon_1 = (\epsilon_s - \epsilon_\infty)_1$, τ_1, α_1 and $\Delta\epsilon_2 = (\epsilon_s - \epsilon_\infty)_2$, τ_2, α_1, α_2 represents the dielectric parameters corresponding to α and β relaxation process, respectively. For the temperatures in the range (2): T = 323–423 K with ΔT = 10 K and for T = 463 K, 473 K, $d_2 = 0$. For the temperatures in the range (3): T = 293–313 K with ΔT = 10 K, $\frac{1}{i\omega\epsilon_0}(\rho_b + E)^{-1} = 0$, and $d_2 = 0$. Hence, from this depiction, there are two relaxations in ASD1; one α process due to cooperative motion of the Qu and PVP, while the other may be due to local motion in the glassy state of ASD1, which can be named as β process. The fit parameters are extracted, and the values obtained for all 19 set temperatures and the results are provided in supplementary Table S1 with magnitude fit quality χ^2, a test that measures how a model compares to actual observed data. Fit results show excellent agreement with measured dielectric dispersion and absorption, and these are shown in Fig. 8(a)-(b), respectively. For further dielectric data representations and detailed analyses on equivalent circuits (Figure S1), the other representations of real and imaginary parts of measured data and fitting *i.e.*, $M^*(\omega)$ in Figure S2, $\sigma^*(\omega)$ in Figure S3, and log(tan(δ)) in Figure S4.a, ϕ in Figure S4.b, and fitting details in Figure S6 refer to the supplementary materials.

The real and imaginary parts of dielectric data of ASD1 on heating from 293 K to 473 K with a difference of 10 K were displayed in Fig. 8.a-b for 19 different temperatures. At high temperatures, especially when samples melt, in lower frequencies, a sudden hike in the dielectric strength was observed in Fig. 8.a, which may be due to EE. This EE masks the relaxation process in the dielectric spectra. In Fig. 8.b, a weak broad relaxation can be visible at the higher frequency side. As the temperature increases, these relaxations shift to higher frequencies; this may indicate a secondary relaxation.

Fig. 9 depicts the temperature dependence of relaxation times of all process in ASD1. The magenta data points in the high-temperature region exhibit nonlinear behaviour in the relaxation map, characteristic of the α-relaxation process due to cooperative motion of miscible Qu and PVP. However, the blue data points also show a linear dependence with two slopes, which may be attributed to the local segmental motion of the ASD. The τ_β relaxation was modelled using the equation: $\tau_\beta =$

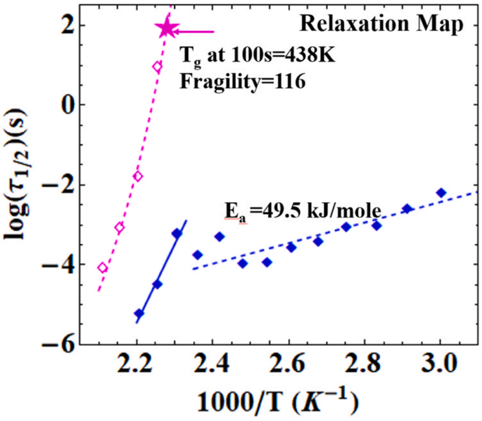

Fig. 9. The temperature dependence of the relaxation times of α and β process.

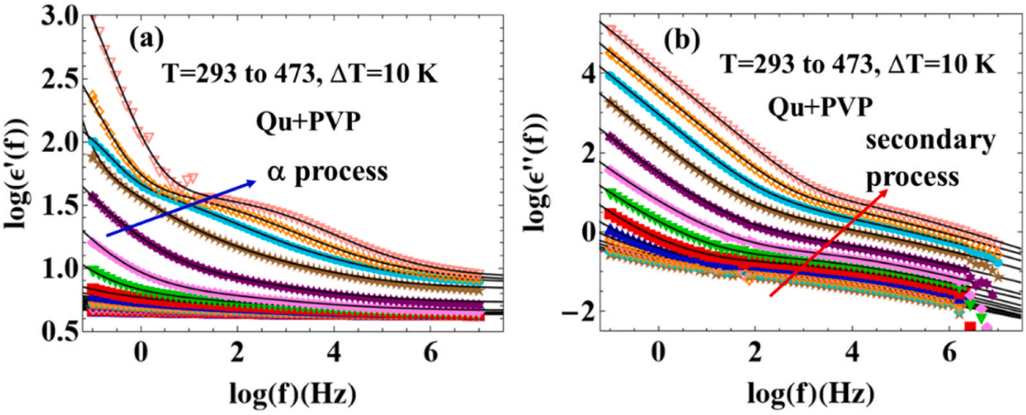

Fig. 8. Frequency-dependent dielectric response of the optimized ASD1 (Qu+PVP) formulation measured during heating from 293 K to 473 K with a temperature interval of 10 K over the frequency range of 10^{-2} to 10^7 Hz in log–log scale: (a) real part (ε') showing the α-relaxation process, and (b) imaginary part (ε'') representing the secondary relaxation process related to localized dipolar dynamics. Symbols represent experimental data, while solid lines correspond to simultaneous fitting of $\epsilon'(f)$ and $\epsilon''(f)''$ using the proposed model described in Eq. (1).

$\tau_{\infty}\exp\left(\frac{Ea}{RT}\right)$, where, E_a is the activation energy, R is the universal gas constant and T is the absolute temperature. The relaxation times display three distinct regimes: a linear Arrhenius-like behaviour at lower temperatures 333 K to 423 K, characterized by an activation energy of E_a = 49.5 kJ/mol, suggesting localized dipolar motions; a super-Arrhenius increase in τ near the glass transition (433 K to 453 K); and a non-Arrhenius trend attributed to cooperative molecular motions in ASD1. The non-Arrhenius τ_α can be described by the Vogel-Fulcher-Tammann (VFT). The VFT equation captures the dramatic increase in relaxation time as the system approaches the glass transition temperature and is expressed as: [63,64]

$$\tau(T) = \tau_0 \exp\left(\frac{A}{(T - T_0)}\right)$$

where, τ(T) represents the relaxation time at temperature T, τ_0 is the pre-exponential factor, A is a parameter related to the apparent activation energy, and T_0 is the Vogel temperature—often interpreted as the temperature at which the relaxation time would diverge. The obtained parameters by fitting the experimental data to the VFT model are A, τ_0 and T_0 and provide insight into the cooperative molecular dynamics occurring near the glass transition region. The fragility index m can be calculated to further characterize the system's glass-forming behavior. This index quantifies how sharply the relaxation time increases as the system approaches the glass transition temperature (T_g). A higher fragility index (m>80) indicates a more dramatic increase in relaxation time, characteristic of fragile glass-formers, whereas lower values (m<50) suggest a stronger, more Arrhenius-like behaviour [43–46]. Mathematically, the fragility index m is defined as the slope of $\log_{10}\tau$ with respect to the reduced temperature $\frac{Tg}{T}$ evaluated at $T = T_g$ as follows [65,66]

$$m = \left(\frac{d\log_{10}\tau}{d\left(\frac{T_g}{T}\right)}\right)_{T= \quad T_g} = \frac{A}{(T_g - T_0)^2}\frac{T_g}{\ln 10}$$

The glass transition temperature (T_g) is evaluated from the relaxation map as Tg = 438 K, the temperature at which the relaxation time (τ) reaches 100 s, which is indicated by a pink star in the map. The fragility was calculated from the VFT parameters using the expression for m, as stated in the theoretical modelling section, and is found to be 116. This steepness index indicates a moderate to high temperature dependence of molecular mobility near the glass transition temperature. It is crucial to store the formulation at a temperature significantly below its glass transition temperature (T_g) to ensure long-term physical stability, minimize molecular mobility, and prevent recrystallization. In the present study, the observed high T_g of the formulation indicates sufficient thermal stability, allowing storage at ambient (room) temperature without compromising its amorphous nature. This contributes to an extended shelf life and maintains the desired physicochemical properties over time.

3.7. Antioxidant activity

3.7.1. DPPH radical scavenging activity

The DPPH assay depicted in Fig. 10.a, demonstrated a concentration-dependent increase in radical scavenging activity for all samples (2–10 μM). However, significant differences were observed among the formulations.

At 2 μM, Qu in water showed minimal inhibition (~0.5%), whereas ASD1 in water exhibited slightly higher activity (~3.6%), and Qu in DMSO showed ~12.69% inhibition. With increasing concentrations, the difference became more pronounced. At 6 μM, Qu in water achieved ~1% inhibition, while ASD1 in water showed ~16%, compared to ~40% for Qu in DMSO. At the highest concentration (10 μM), Qu in water showed ~3% inhibition, ASD1 in water ~24%, and Qu in DMSO reached ~65% inhibition. The improved activity of ASD1 in water compared to pure Qu in water can be attributed to enhanced solubility of Qu in the amorphous solid dispersion (ASD). Due to poor aqueous solubility, free Qu in water remains partially undissolved, limiting the number of available antioxidant molecules to interact with DPPH radicals. In contrast, ASD1 increases molecular dispersion of Qu, thereby increasing the number of bioavailable Qu molecules in solution. This enhanced molecular availability directly correlates with increased hydrogen-donating capacity and higher radical scavenging efficiency.

3.7.2. Superoxide radical scavenging activity

Similar trends were observed in the superoxide radical scavenging assay (20–100 μM) depicted in Fig. 10.b. The activity increased dose-dependently across all groups. At 20 μM, Qu in water showed ~2.4% inhibition, whereas ASD1 in water exhibited ~6.8%, and Qu in DMSO showed ~10%. At 60 μM, Qu in water reached ~4.42%, ASD1 in water increased to ~25%, and Qu in DMSO achieved ~35%. At 100 μM, Qu in water demonstrated ~10% inhibition, while ASD1 in water significantly improved to ~37%, and Qu in DMSO reached ~58%. The marked enhancement in ASD1 is again attributed to increased aqueous solubility and improved molecular dispersion. Superoxide scavenging requires effective interaction between Qu hydroxyl groups and reactive oxygen species. In aqueous medium, limited dissolution restricts this interaction

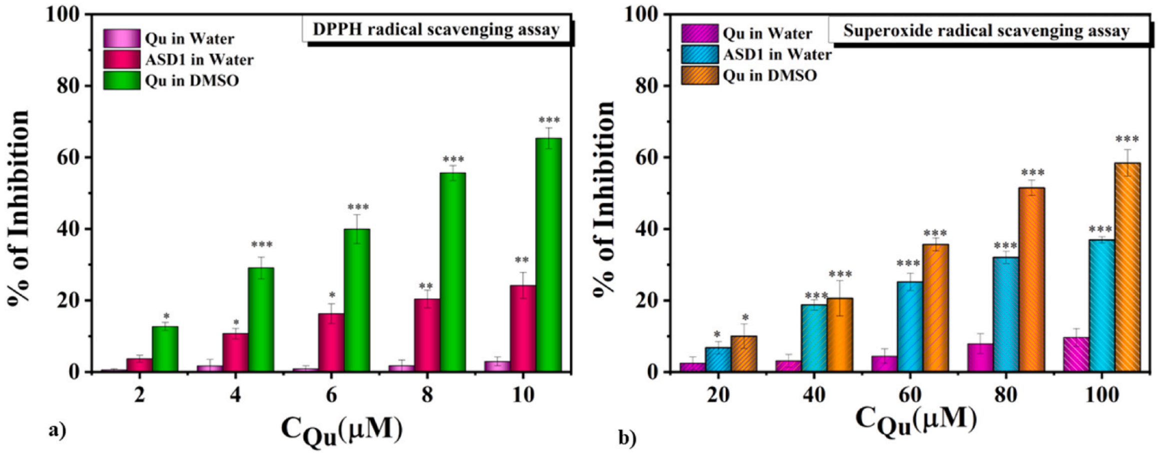

Fig. 10. *In vitro* antioxidant activity of Qu and ASD1 formulations. (a) DPPH radical scavenging activity of Qu in water, ASD1 in water, and Qu in DMSO at the concentrations of 2–10 μM. (b) Superoxide radical scavenging activity of Qu in water, ASD1 in water, and Qu in DMSO at the concentrations of 20–100 μM. Data are presented as mean ± SD (n = 3). Statistical significance is indicated as $p < 0.05$ (*), $p < 0.01$ (**), and $p < 0.001$ (***).

for pure Qu. ASD1 enhances drug wettability and reduces crystallinity, leading to improved dissolution and increased availability of active antioxidant moieties.

3.8. Anti-inflammatory activity

The anti-inflammatory potential of Qu and the ASD1 formulation was assessed using the nitric oxide (NO) scavenging assay. The percent of inhibition graph is depicted in Fig. 11. All samples demonstrated concentration-dependent nitric oxide scavenging activity. However, significant differences were observed among the formulations, as observed in DPPH. At lower concentration (20 μM), Qu in water exhibited minimal inhibition (~0.12%), whereas ASD1 in water showed higher inhibition (~3.17%), indicating improved availability of active molecules. Qu in DMSO demonstrated slightly higher inhibition (~17%) due to complete solubilization. At intermediate concentrations (60 μM), Qu in water showed moderate inhibition (~0.6%), while ASD1 in water significantly increased inhibition to ~15.7%. In contrast, Qu in DMSO reached ~31% inhibition.

At the highest concentration tested (10 μM), Qu in water demonstrated approximately ~1.2% inhibition, whereas ASD1 in water exhibited markedly enhanced activity (~28). Qu in DMSO showed the highest inhibition (~51%), serving as the solubility-maximized reference. The enhanced nitric oxide scavenging activity of ASD1 compared to pure Qu in water can be directly attributed to improved aqueous solubility and increased molecular dispersion of Qu in the amorphous solid dispersion. Poorly soluble crystalline Qu limits the number of free hydroxyl groups available to neutralize reactive nitrogen species. In contrast, ASD1 enhances dissolution, thereby increasing the number of bioavailable Qu molecules capable of interacting with and scavenging nitric oxide radicals.

3.9. Anti-proliferative activity

ASD1 was selected as the representative formulation for cytotoxicity evaluation on the basis of its superior physicochemical performance among the prepared ASDs. MCF-7 and MDA-MB-231 are two widely used human breast cancer cell lines that represent distinct molecular subtypes of breast cancer. MCF-7 cells are hormone receptor–positive (ER^+), whereas MDA-MB-231 cells are classified as triple-negative breast cancer (TNBC), lacking estrogen receptor (ER), progesterone receptor (PR), and HER2 expression. Because TNBC does not express these three receptors, it is more aggressive and difficult to treat with conventional targeted therapies. Due to their contrasting biological characteristics, the combined use of MCF-7 and MDA-MB-231 provides a robust *in vitro* platform for evaluating novel anticancer agents across different breast cancer subtypes. In particular, MDA-MB-231 cells are valuable for studying therapies that can bypass receptor-mediated pathways, while MCF-7 cells help assess responses in hormone-responsive tumors.

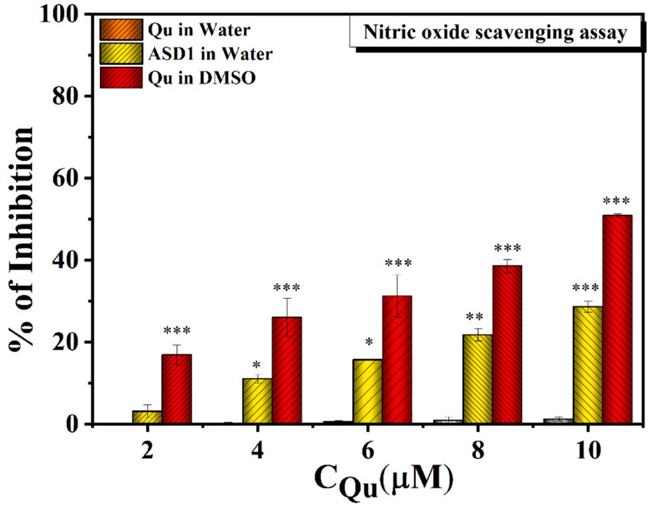

Fig. 11. *In vitro* anti-inflammatory activity evaluated by nitric oxide (NO) assay. Percentage inhibition of NO production by Qu and ASD1 in water, and Qu in DMSO at varying concentrations (e.g., 20–100 μM). Data are presented as mean ± SD (n = 3). Statistical significance is indicated as $p < 0.05$ (*), *$p < 0.01$ (**), and $p < 0.001$ (***).*

3.10. MDA-MB-231 cell

The Fig. 12 illustrates a dose-dependent inhibition of MDA-MB-231 cell growth by Qu and its ASD1. The percentage of inhibition were plotted in Fig. 13.a. Qu in water (cyan) exhibited the least cytotoxicity, attributed to its poor aqueous solubility with inhibition percentages remaining below 25% even at the highest concentration. While Qu in ethanol (green) and ASD1 in water (yellow) showed moderate inhibition. The percentage inhibition was notably enhanced in the formulated ASD1; the efficacy of ASD1 in water reached 45% and ASD1 in ethanol (red bars) exhibited the highest cytotoxic effect in all concentrations, reaching nearly 90% inhibition at 100 μM. This enhancement of the antiproliferative effect of ASD1 in water and ethanol suggests that the formulation not only improved the solubility and dispersion of Qu but also significantly enhanced its bioavailability and cytotoxic potential. Notably, the superior performance of ASD1 in ethanol over Qu in DMSO highlights the efficiency of the amorphous dispersion approach in improving the therapeutic efficacy of poorly water-soluble natural compounds like Qu in aggressive.

The calculated IC_{50} values of Qu and prepared ASD1 in different solvents were tabulated in Table 4. The IC_{50} of pure Qu in water (203.27 ± 0.5* μM, obtained from extrapolation of fitting) was not achieved even at 100 μM, reflecting its extremely poor aqueous solubility. In contrast, Qu in DMSO demonstrated the highest potency among the non-formulated forms, with IC_{50} values of 62.3 ± 1.16 μM, highlighting DMSO's ability to enhance bioavailability through solubilization. Ethanol moderately improved efficacy 75.45 ± 3.4 μM for MDA-MB-231.

The ASD1 formulation significantly improved cytotoxicity in aqueous and ethanolic media. While the IC_{50} of ASD1 in water most probably reach 106 ± 3.7* μM. Notably, ASD1 in ethanol achieved IC_{50} value of 40.54 ± 0.55 μM, outperforming pure Qu in both ethanol and DMSO against MDA-MB-231 cell line. These results clearly demonstrate that the ASD1 formulation enhances the cytotoxic potential of Qu, likely by improving solubility, dispersibility, and cellular uptake, thereby offering a promising approach for developing more effective anticancer therapies against aggressive breast cancers. This superior performance of ASD1 underscores the critical role of amorphous formulation in improving solubility, cellular uptake, and overall bio efficacy of hydrophobic natural compounds such as Qu. These findings support the potential of ASD1 as a promising therapeutic candidate for cancer treatment.

3.10.1. MCF-7 cell line

Fig. 14 illustrates the morphological changes observed in MCF-7 breast cancer cells treated with Qu and its ASD1 formulation across different solvent systems, water, ethanol, and DMSO, at increasing concentrations of 20, 60, 80, and 100 μM, as visualized under 10X phase-contrast microscopy and their percentage of inhibition were plotted in Fig. 13.b.

Upon treatment, progressive dose-dependent morphological alterations of cells were evident across all formulations, including cell rounding, shrinkage, loss of confluence, and detachment from the culture surface, indicative of cytotoxic activity.

Qu in water exhibited the least morphological disruption, consistent with its poor aqueous solubility, even at 100 μM. Qu in ethanol induced moderate morphological changes, with reduction in cell density at

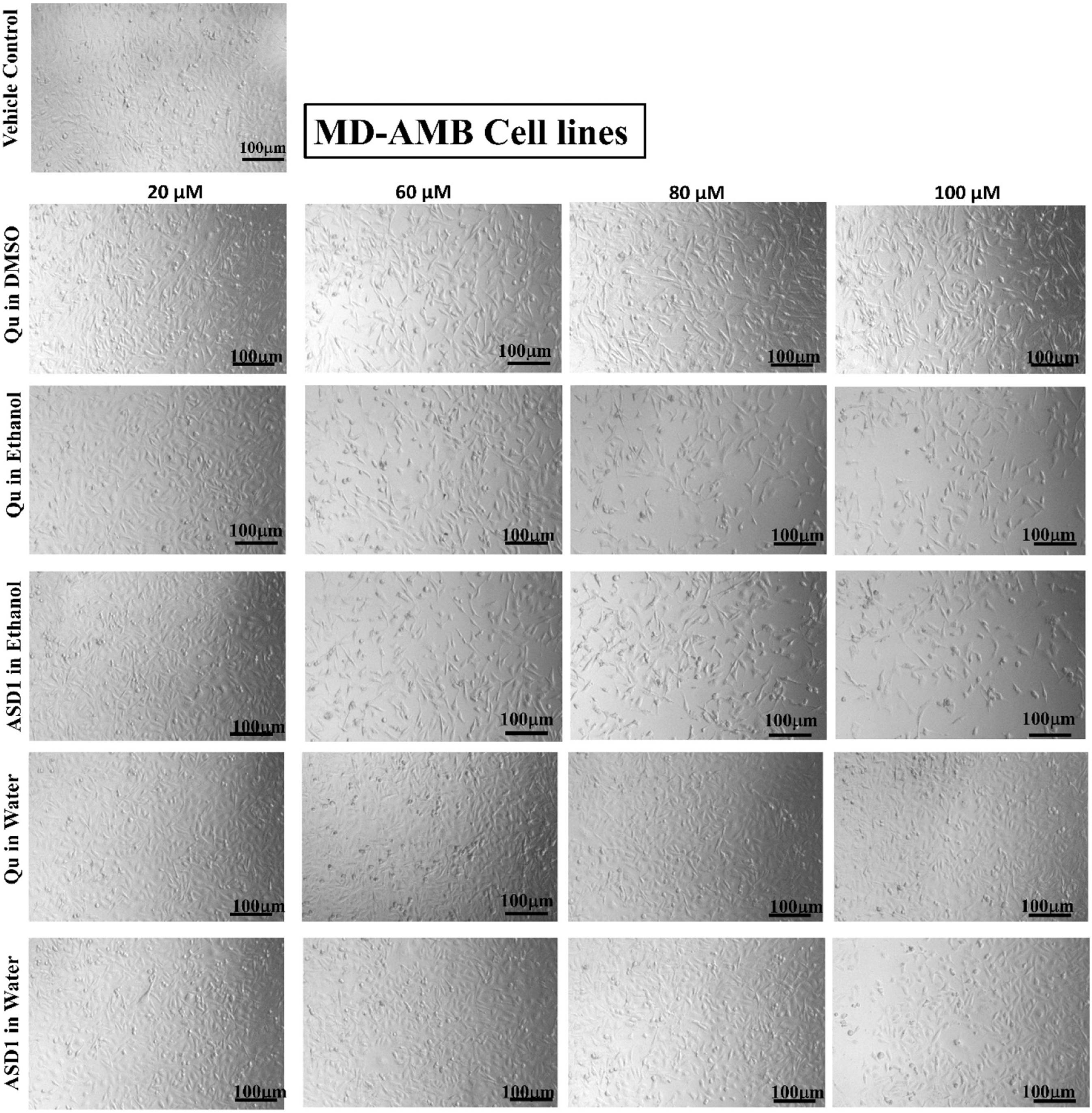

Fig. 12. Microscopic images taken at a magnification of 10X showing morphological changes in MDA-MB-231 breast cancer cells treated with increasing concentrations (20, 60, 80, and 100 μM) of different formulations. Row: vehicle (water) control, Qu in DMSO, Qu in ethanol, ASD1 in ethanol, Qu in water, ASD1 in water.

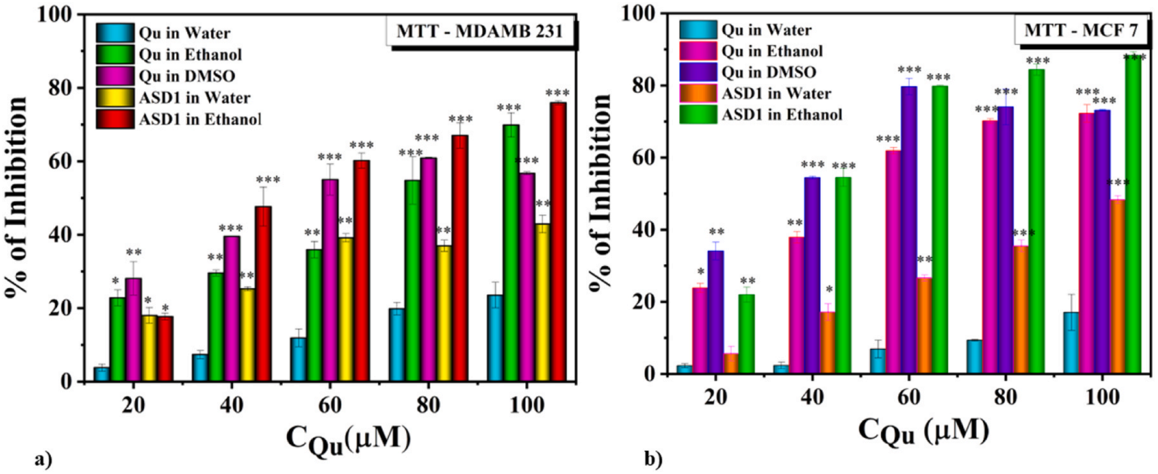

Fig. 13. *In vitro* cytotoxic activity of Qu and ASD1 formulations in different solvents (water, ethanol, DMSO) against a) MDAMB-231 and b) MCF-7 breast cancer cell lines as measured by MTT assay. The percentage of inhibition is plotted against increasing concentrations of Qu ranging from 20 to 100 μM.

Table 4
IC_{50} values (μM) of Qu and its optimized ASD1 formulated in different solvent systems against MDA-MB-231 and MCF-7 breast cancer cell lines, determined by MTT assay. Data are expressed as mean ± SEM (n = 3).

Sl.No	Sample	MDA-MB-231 cell line	MCF-7 cell line
		IC_{50} Values (μM)	IC_{50} Values (μM)
1	Qu in water	203.27 ± 0.5*	409.88 ± 0.56*
2	Qu in ethanol	75.45 ± 3.4	35.9 ± 1.28
3	Qu in DMSO	62.3 ± 1.16	32.04 ± 1.13
4	ASD1 in water	106 ± 3.7*	104.72 ± 1.29*
5	ASD1 in ethanol	40.54 ± 0.55	39.08 ± 0.55

* IC_{50} values were determined by linear fitting of the dose–response data and extrapolation of the fitted curve. The corresponding plots are provided in the Figure S9 in supplementary material.

higher concentrations. Qu in DMSO demonstrated comparatively greater cytotoxic and morphological effects among the non-formulated variants, reflecting DMSO-mediated solubilization enhancing drug availability to cells. Notably, ASD1 formulations produced markedly superior morphological disruption relative to their respective pure Qu counterparts. ASD1 in ethanol caused progressive and pronounced cell loss, rounding, and detachment across all concentrations, with near-complete disruption of the monolayer at 100 μM. ASD1 in water, while showing lesser activity compared to the ethanolic form, demonstrated visibly greater cytotoxic morphological changes than pure Qu in water, reflecting the formulation's capacity to improve aqueous dispersibility and cellular exposure.

The IC_{50} values calculated from the MCF-7 viability data are presented in Table 3. Pure Qu in water failed to achieve an IC_{50} within the tested concentration range of up to 100 μM (IC_{50} estimated at 409.88 ± 0.56* μM), underscoring its limited aqueous solubility and consequent poor cytotoxic potency. Qu in ethanol and DMSO yielded IC_{50} values of 35.9 ± 1.28 μM and 32.04 ± 1.13 μM, respectively, with DMSO again demonstrating the highest potency among non-formulated groups due to its solubilizing effect. Similarly, ASD1 in water did not reach IC_{50} within 100 μM (IC_{50} estimated at 104.72 ± 1.29* μM), yet showed a meaningful improvement over pure Qu in water, indicating partial but significant enhancement in aqueous dispersibility and cellular uptake. ASD1 in ethanol achieved an IC_{50} of 39.08 ± 0.55 μM, outperforming pure Qu in both ethanol and water, and approaching the potency of Qu in DMSO, which is particularly significant given that ethanol represents a more biologically relevant and pharmaceutically acceptable solvent system than DMSO. These findings collectively demonstrate that ASD1 substantially enhances the antiproliferative efficacy of Qu in MCF-7 cells, likely through improved solubility, wettability, and cellular bioavailability conferred by the ASD approach.

4. Conclusion

The study demonstrated that formulating Qu as ASD with PVP effectively addresses its inherent limitations like poor solubility, low bioavailability, and instability, characteristic of BCS Class IV drugs. Among the tested ratios, ASD1 (1:9; Qu:PVP) exhibited optimal performance, as confirmed by physicochemical analyses including DSC, SEM, XRD, FTIR, TGA, and BDS. XRD confirmed complete amorphization in ASD1, while solubility studies showed a significant enhancement from 0.53 μM in water for pure Qu to 25.83 μM for ASD1. TGA and DSC results indicated improved thermal stability and a distinct glass transition at 395 K, supported by dielectric spectroscopy, which further revealed dynamic stability with a fragility index of 116. The antioxidant and anti-inflammatory assays demonstrated markedly higher inhibition with ASD1, 24% vs 3% (DPPH, 10 μM), 37% vs 10% (superoxide, 100 μM), and 28% vs 1.2% (NO, 100 μM) compared to quercetin in water, highlighting enhanced molecular availability, improved solubility, and superior bioactivity achieved through amorphization. Importantly, cytotoxicity studies on MCF-7 and MDA-MB-231 cells demonstrated markedly higher inhibition with ASD1, approximately 90% in ethanol and 45% in water, compared to Qu alone, this enhancement may be attributed to increased molecular availability of quercetin in ASD1 due to improved solubility and dispersion. These findings suggest that ASD offers a promising strategy to harness the anticancer potential of poorly soluble natural compounds like Qu in breast cancer, including aggressive TNBC treatment.

Author contributions

Davis Anu and K.P. Safna Hussan contributed equally to this work. D. A. was responsible for *in vitro* anticancer assays. K.P.S.H. conceptualized the study, formulated the development, characterized the physicochemical properties, interpreted the dielectric spectroscopy data, and drafted the manuscript. Natália T. Correia and Florence Danède contributed to thermal and dielectric measurements (TGA, DSC and BDS) and critically revised the manuscript. G. Govindaraj provided support for data analysis using Mathematica. S. Lekshmi and Gowri Kalyani assisted in datafitting. Naoki Shinyashiki supervised dielectric spectroscopy experiments and contributed to the analysis of molecular dynamics and relaxation behavior. Thekkekara D. Babu provided overall guidance and a critical review of the manuscript.

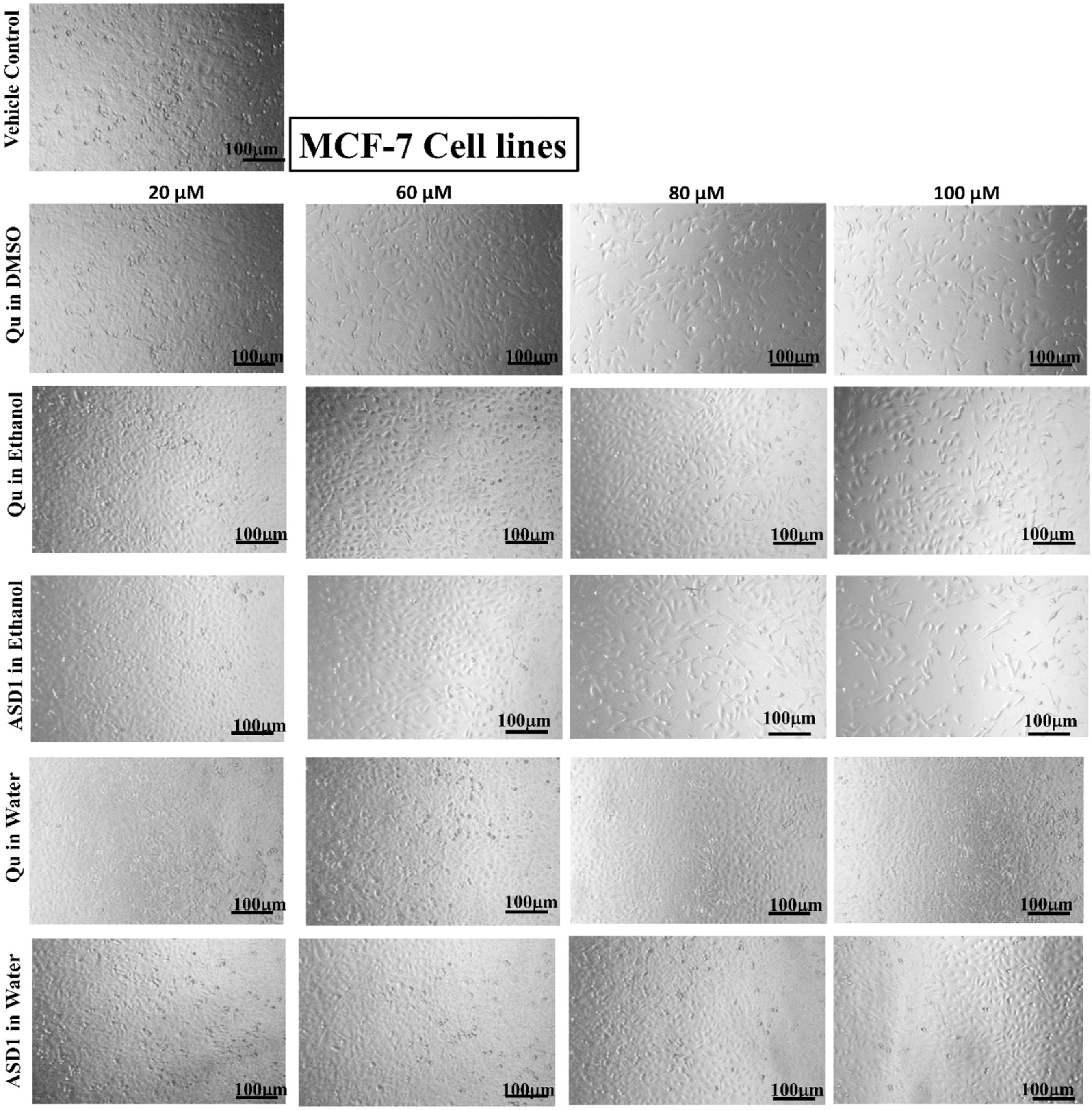

Fig. 14. Microscopic images taken at a magnification of 10X showing morphological changes in MCF-7 breast cancer cells treated with increasing concentrations (20, 60, 80, and 100 μM) of different formulations. Row: evhicle control (water), Qu in DMSO, Qu in Ethanol, ASD1 in Ethanol, Qu in water, ASD1 in water.

CRediT authorship contribution statement

Davis Anu: Methodology, Formal analysis, Data curation. **K. P Safna Hussan:** Writing – original draft, Investigation, Formal analysis, Data curation, Conceptualization. **Florence Danède:** Data curation. **Natália T. Correia:** Writing – review & editing, Software, Data curation. **T.D Babu:** Writing – review & editing, Validation, Supervision, Formal analysis, Data curation. **S. Lekshmi:** Writing – review & editing, Visualization. **G. Govindaraj:** Writing – review & editing, Software, Investigation. **Naoki Shinyashiki:** Writing – review & editing, Supervision, Software, Funding acquisition. **Gowri Kalyani:** Formal analysis, Data curation.

Declaration of Competing Interest

The authors declare that they have no known competing financial interests or personal relationships that could have appeared to influence the work reported in this paper.

Appendix A. Supporting information

Supplementary data associated with this article can be found in the online version at doi:10.1016/j.mtcomm.2026.115019.

Data availability

Data will be made available on request.

References

[1] H. Nishimuro, H. Ohnishi, M. Sato, M. Ohnishi-kameyama, I. Matsunaga, S. Naito, K. Ippoushi, H. Oike, T. Nagata, H. Akasaka, S. Saitoh, K. Shimamoto, M. Kobori, Estimated daily intake and seasonal food sources of quercetin in Japan, Nutrients (2015) 2345–2358, https://doi.org/10.3390/nu7042345.

[2] Aikaterini-Spyridoula Michala, Agathi Pritsa, Quercetin: a molecule of great biochemical and clinical value, Diseases (2022).

[3] A. Rauf, M. Imran, I. Ali, K. Mujeeb, Anticancer potential of quercetin: a comprehensive review anticancer potential of quercetin: a comprehensive review, Wile (2018), https://doi.org/10.1002/ptr.6155.

[4] Z. Wu, Quercetin: a natural ally in combating breast quercetin, A Nat. Ally Combat. Breast Cancer 9114 (2025), https://doi.org/10.2147/IJN.S518174.

[5] K.P.S. Hussan, A. Davis, S. Lekshmi, M. Shahin, A. Chathrattil, T. Devassy, Evaluation of the binding efficacy of flavonol derivatives on estrogen receptors (ER) with respect to ring B hydroxylation, Results Chem. 7 (2024) 101544, https://doi.org/10.1016/j.rechem.2024.101544.

[6] G. Wang, Y. Wang, L. Yao, W. Gu, S. Zhao, Z. Shen, Z. Lin, W. Liu, T. Yan, Pharmacological Activity of Quercetin, Update Rev. 2022 (2022), https://doi.org/10.1155/2022/3997190.

[7] H. Zou, H. Ye, R. Kamaraj, T. Zhang, J. Zhang, P. Pavek, A review on pharmacological activities and synergistic effect of quercetin with small molecule agents, Phytomedicine 92 (2021) 153736, https://doi.org/10.1016/j.phymed.2021.153736.

[8] M. Shahbaz, H. Naeem, U. Momal, M. Imran, S.A. Alsagaby, W. Al Abdulmonem, A. B. Waqar, H. Ahmed, M.M. Ghoneim, M.A. Abdelgawad, E. Shaker, M. Umar, M. Hussain, R. Kumar, E. Al, M. Shahbaz, H. Naeem, U. Momal, M. Imran, S. A. Alsagaby, W. Al Abdulmonem, A.B. Waqar, A.H. El-ghorab, M.M. Ghoneim, M. A. Abdelgawad, M.E. Shaker, M. Umar, H. Naeem, U. Momal, M. Imran, S. A. Alsagaby, W. Al Abdulmonem, A. Bilal, A.H. El-ghorab, M. Ghoneim, M. A. Abdelgawad, Anticancer and apoptosis inducing potential of quercetin against a wide range of human malignancies, Int. J. Food Prop. 26 (2023) 2590–2626, https://doi.org/10.1080/10942912.2023.2252619.

[9] C. Chen, J. Zhou, C. Ji, Quercetin: a potential drug to reverse multidrug resistance, Life Sci. 87 (2010) 333–338, https://doi.org/10.1016/j.lfs.2010.07.004.

[10] W. Xu, S. Xie, X. Chen, S. Pan, H. Qian, X. Zhu, Effects of quercetin on the efficacy of various chemotherapeutic drugs in cervical cancer cells, Drug Des. Devel. Ther. (2021) 577–588.

[11] S. Li, K. Li, J. Zhang, Z. Dong, The effect of quercetin on doxorubicin cytotoxicity in human breast cancer cells, AntiCancer Agents Med. Chem. (Formerly Curr. Med. Chem. Agents 13 (2013) 352–355.

[12] R. Wang, L. Yang, S. Li, D. Ye, L. Yang, Q. Liu, Z. Zhao, Q. Cai, J. Tan, X. Li, Quercetin inhibits breast cancer stem cells via downregulation of aldehyde dehydrogenase 1A1 (ALDH1A1), chemokine receptor type 4 (CXCR4), mucin 1 (MUC1), and epithelial cell adhesion molecule (EpCAM), Med. Sci. Monit. 24 (2018) 412–420, https://doi.org/10.12659/MSM.908022.

[13] B. Dilek, Ö. Meltem, Quercetin suppresses cell proliferation using the apoptosis pathways in MCF-7 and MDA-MB-231 human breast carcinoma cells in monolayer and spheroid model cultures: Effect of Quercetin on Human Breast Cancer, South Afr. J. Bot. 162 (2023) 259–270, https://doi.org/10.1016/j.sajb.2023.09.017.

[14] J. Jiang, Y. Yang, F. Wang, W. Mao, Z. Wang, Z. Liu, Quercetin inhibits breast cancer cell proliferation and survival by targeting Akt/mTOR/PTEN signaling pathway, Chem. Biol. Drug Des. 103 (2024) e14557.

[15] S. Ranganathan, D. Halagowder, N.D. Sivasithambaram, Quercetin suppresses twist to induce apoptosis in MCF-7 breast cancer cells, PLoS One 10 (2015) 1–12, https://doi.org/10.1371/journal.pone.0141370.

[16] C.-W. Lin, W.-C. Hou, S.-C. Shen, S.-H. Juan, C.-H. Ko, L.-M. Wang, Y.-C. Chen, Quercetin inhibition of tumor invasion via suppressing PKCδ/ERK/AP-1-dependent matrix metalloproteinase-9 activation in breast carcinoma cells, Carcinogenesis 29 (2008) 1807–1815, https://doi.org/10.1093/carcin/bgn162.

[17] L. Fang, D. Gao, T. Wang, H. Zhao, Y. Zhang, S. Wang, From nature to clinic: Quercetin's role in breast cancer immunomodulation, Front. Immunol. 15 (2024) 1–14, https://doi.org/10.3389/fimmu.2024.1483459.

[18] P. Han, S. Chu, J. Shen, L. Li, Y. Zhang, S. Wang, Y. Chen, Y. Ma, X. Tang, C. Gao, Quercetin-derived microbial metabolite DOPAC potentiates CD8+ T cell anti-tumor immunity via NRF2-mediated mitophagy, Cell Metab. 37 (2025) 2438–2454.

[19] N.G. Sannappa Gowda, V.D. Shiragannavar, L.D. Puttahanumantharayappa, A. T. Shivakumar, S. Dallavalasa, C.G. Basavaraju, S.S. Bhat, S.K. Prasad, R. M. Vamadevaiah, S.R.V. Madhunapantula, P.K. Santhekadur, Quercetin activates vitamin D receptor and ameliorates breast cancer induced hepatic inflammation and fibrosis, Front. Nutr. 10 (2023) 1–12, https://doi.org/10.3389/fnut.2023.1158633.

[20] K. Kandemir, M. Tomas, D.J. McClements, E. Capanoglu, Recent advances on the improvement of quercetin bioavailability, Trends Food Sci. Technol. 119 (2022) 192–200, https://doi.org/10.1016/j.tifs.2021.11.032.

[21] X. Chen, O.Q.P. Yin, Z. Zuo, M.S.S. Chow, Pharmacokinetics and Modeling of Quercetin and Metabolites: Chen, Yin, Zuo, and Chow, Pharm. Res. 22 (2005) 892–901.

[22] G.C. Justino, M.R. Santos, S. Canário, C. Borges, M.H. Florêncio, L. Mira, Plasma quercetin metabolites: Structure-antioxidant activity relationships, Arch. Biochem. Biophys. 432 (2004) 109–121, https://doi.org/10.1016/j.abb.2004.09.007.

[23] X. Zhu, G. Ding, S. Ren, J. Xi, K. Liu, The bioavailability, absorption, metabolism, and regulation of glucolipid metabolism disorders by quercetin and its important glycosides: A review, Food Chem. 458 (2024) 140262.

[24] A. Fusina, P. Degot, D. Touraud, W. Kunz, V. Nardello-Rataj, Enhancement of water solubilization of quercetin by meglumine and application of the solubilization concept to a similar system, J. Mol. Liq. 368 (2022), https://doi.org/10.1016/j.molliq.2022.120756.

[25] H. Li, X. Zhao, Y. Ma, G. Zhai, L. Li, H. Lou, Enhancement of gastrointestinal absorption of quercetin by solid lipid nanoparticles, J. Control. Release 133 (2009) 238–244.

[26] P. Zhou, W. Liu, Y. Cheng, D. Qian, Nanoparticle-based applications for cervical cancer treatment in drug delivery, gene editing, and therapeutic cancer vaccines, Wiley Interdiscip. Rev. Nanomed. Nanobiotechnol. 13 (2021) e1718.

[27] N.P. Gullett, A.R.M. Ruhul Amin, S. Bayraktar, J.M. Pezzuto, D.M. Shin, F.R. Khuri, B.B. Aggarwal, Y.J. Surh, O. Kucuk, Cancer prevention with natural compounds, Semin. Oncol. 37 (2010) 258–281, https://doi.org/10.1053/j.seminoncol.2010.06.014.

[28] Y. Ma, C. Yao, H. Liu, F. Yu, J. Lin, K. Lu, C. Liao, F. Chueh, J. Chung, Quercetin induced apoptosis of human oral cancer SAS cells through mitochondria and endoplasmic reticulum mediated signaling pathways, Oncol. Lett. 15 (2018) 9663–9672.

[29] J.K. Paul, M. Azmal, A.S.N.B. Haque, O.F. Talukder, M. Meem, A. Ghosh, Phytochemical-mediated modulation of signaling pathways: a promising avenue for drug discovery, Adv. Redox Res. 13 (2024) 100113, https://doi.org/10.1016/j.arres.2024.100113.

[30] J. Lu, Z. Wang, S. Li, Q. Xin, M. Yuan, H. Li, X. Song, H. Gao, N. Pervaiz, X. Sun, W. Lv, T. Jing, Y. Zhu, Quercetin inhibits the migration and invasion of HCCLM3 cells by suppressing the expression of p-Akt1, matrix metalloproteinase (MMP) MMP-2, and MMP-9, Med. Sci. Monit. 24 (2018) 2583–2589, https://doi.org/10.12659/MSM.906172.

[31] D.J. Kwon, S.M. Ju, G.S. Youn, S.Y. Choi, J. Park, Suppression of iNOS and COX-2 expression by flavokawain A via blockade of NF-κB and AP-1 activation in RAW 264.7 macrophages, Food Chem. Toxicol. 58 (2013) 479–486, https://doi.org/10.1016/j.fct.2013.05.031.

[32] Y.H. Jung, J. Heo, Y.J. Lee, T.K. Kwon, Y.H. Kim, Quercetin enhances TRAIL-induced apoptosis in prostate cancer cells via increased protein stability of death receptor 5, Life Sci. 86 (2010) 351–357, https://doi.org/10.1016/j.lfs.2010.01.008.

[33] S. Tambe, D. Jain, S.K. Meruva, G. Rongala, A. Juluri, G. Nihalani, H.K. Mamidi, P. K. Nukala, P.K. Bolla, Recent advances in amorphous solid dispersions: preformulation, formulation strategies, technological advancements and characterization, Pharmaceutics 14 (2022) 2203.

[34] S. B, A. Ghosh, Mechanistic insights into amorphous solid dispersions: bridging theory and practice in drug delivery, Pharm. Res. 42 (2025) 1–23, https://doi.org/10.1007/s11095-024-03808-w.

[35] Z. Fan, H. Iqbal, J. Ni, N.U. Khan, S. Irshad, A. Razzaq, M.Y. Alfaifi, S.E.I. Elbehairi, A.A. Shati, J. Zhou, Rationalized landscape on protein-based cancer nanomedicine: Recent progress and challenges, Int. J. Pharm. X 7 (2024) 100238.

[36] C. Luo, R. Li, M. Tang, Y. Gao, J. Zhang, S. Qian, Y. Wei, P. Shen, Amorphous solid dispersion to facilitate the delivery of poorly water-soluble drugs: recent advances on novel preparation processes and technology coupling, Expert Opin. Drug Deliv. 21 (2024) 1807–1822.

[37] J. Han, M. Tang, Y. Yang, W. Sun, Z. Yue, Y. Zhang, Y. Zhu, X. Liu, J. Wang, Amorphous solid dispersions: stability mechanism, design strategy and key production technique of hot melt extrusion, Int. J. Pharm. 646 (2023) 123490.

[38] J.A. Marks, B.L.B. Nichols, L.I. Mosquera-Giraldo, S.T. Yazdi, L.S. Taylor, K. J. Edgar, 6-Carboxycellulose acetate butyrate: effectiveness as an amorphous solid dispersion polymer, Mol. Pharm. 21 (2024) 4589–4602.

[39] A. Saberi, M. Kouhjani, D. Yari, A. Jahani, K. Asare-Addo, H. Kamali, A. Nokhodchi, Development, recent advances, and updates in binary, ternary co-amorphous systems, and ternary solid dispersions, J. Drug Deliv. Sci. Technol. 86 (2023) 104746.

[40] N. Alhajj, N.J. O'Reilly, H. Cathcart, Development and characterization of a spray-dried inhalable ciprofloxacin-quercetin co-amorphous system, Int. J. Pharm. 618 (2022) 121657.

[41] G.P. Andrews, K. Qian, E. Jacobs, D.S. Jones, Y. Tian, High drug loading nanosized amorphous solid dispersion (NASD) with enhanced in vitro solubility and permeability: Benchmarking conventional ASD, Int. J. Pharm. 632 (2023) 122551.

[42] H.P. Bhatta, H.-K. Han, R. Maharjan, S.H. Jeong, Recent techniques to improve amorphous dispersion performance with quality design, physicochemical monitoring, molecular simulation, and machine learning, Pharmaceutics 17 (2025) 1249.

[43] A. Budiman, A.L. Handini, M.N. Muslimah, N.V. Nurani, E. Laelasari, I. S. Kurniawansyah, D.L. Aulifa, Amorphous solid dispersion as drug delivery vehicles in cancer, Polym. (Basel) 15 (2023) 3380.

[44] M. Khuanekkaphan, K. Netsomboon, A. Fristiohady, R. Asasutjarit, Development of quercetin solid dispersion-loaded dissolving microneedles and in vitro investigation of their anti-melanoma activities, Pharmaceutics 16 (2024) 1276.

[45] K.P.Safna Hussan, Y. Okamura, R. Kita, V.K. Rajan, T.D. Babu, N. Shinyashiki, Dynamics and structural study on supercooled liquid and glassy states of lapatinib: A dual inhibitor of EGFR and HER2 tyrosine kinases for cancer therapy, J. Mol. Liq. 437 (2025) 128536, https://doi.org/10.1016/j.molliq.2025.128536.

[46] M. Sahra, T. Mohamed Shahin, A.K. Bansal, K.L. Ngai, M.K. Sulaiman, G. Shete, K. P. Safna Hussan, Dielectric spectroscopic studies of three important active pharmaceutical ingredients - clofoctol, droperidol and probucol, J. Non Cryst. Solids 505 (2019) 28–36, https://doi.org/10.1016/j.jnoncrysol.2018.10.046.

[47] K.P. Safna Hussan, Mohamed Shahin Thayyil, S.K. Deshpande, T.V. Jinitha, K. Manoj, K.L. Ngai, Molecular dynamics, physical and thermal stability of neat amorphous amlodipine besylate and in binary mixture, Eur. J. Pharm. Sci. 119 (2018) 268–278, https://doi.org/10.1016/j.ejps.2018.04.030.

[48] K. Sasaki, K.P.Safna Hussan, R. Kita, T. Ito, Y. Okamura, N. Shinyashiki, Fundamental insights into bulk polyvinylpyrrolidone (PVP): combining DFT, molecular dynamics, and spectroscopic techniques, Chem. Phys. 603 (2026) 113053, https://doi.org/10.1016/j.chemphys.2025.113053.

[49] Safna Hussan K.P, T.D. Babu, Pareeth C.M, G. Joshy, M.S. Thayyil, A. Cancer, A. Nagar, C. Authors, T.D. Babu, Antioxidant activity of erlotinib and gefitinib: theoretical and experimental insights, Free Radic. Res. 56 (2022) 196–208.

[50] K.P. Safna Hussan, T.D. Babu, M.S. Thayyil, T. Sreeshma, A. Archana, Physiochemical characterization and Biological evaluation of Amorphous solid dispersions of Erlotinib HCl; Better Chemotherapeutic Efficacy, Sci. Rep. 15 (2025) 1–17.

[51] K.P. Safna Hussan, C.M. Pareeth, K. Muraleedharan, M. Shahin Thayyil, T.D. Babu, Synthesis, spectroscopic, chemical reactivity, molecular docking, DFT calculations and in-vitro anticancer activity studies of a novel ionic liquid; Metforminium ibuprofenate, J. Mol. Liq. 364 (2022) 120046, https://doi.org/10.1016/j.molliq.2022.120046.

[52] K.P. Safna Hussan, M. Shahin Thayyil, C.M. Pareeth, K. Manoj, T.D. Babu, Molecular dynamics in amorphous double active ionic liquid developed by chemical structural modification of ibuprofen, J. Mol. Liq. 365 (2022) 120072, https://doi.org/10.1016/j.molliq.2022.120072.

[53] S. Cheralayikkal, K. Manoj, K.P.S. Hussan, Formulation and evaluation of a smart drug delivery system of 5- fl uorouracil for pH-sensitive chemotherapy, Heliyon 8 (2022) e09926, https://doi.org/10.1016/j.heliyon.2022.e09926.

[54] R.P. R . , L. Tom, D.N. P . , K.P. Safna Hussan, V.P. Raphael, V.B. Bhagyesh, B. Joseph, Two novel Aroyl Hydrazones from 4-methoxybenzhydrazide: comprehensive study including synthesis, X-ray crystallography, DFT analysis, antibacterial activity and molecular docking, J. Mol. Struct. 1335 (2025) 141866, https://doi.org/10.1016/j.molstruc.2025.141866.

[55] E. Codomiu-Hernández, A. Mesa-Ibirico, L.A. Montero-Cabrera, F. Martínez-Luzardo, T. Borrmann, W.D. Stohrer, Theoretical study of flavonoids and proline interactions. Aqueous and gas phases, J. Mol. Struct. THEOCHEM 623 (2003) 63–73, https://doi.org/10.1016/S0166-1280(02)00663-2.

[56] K. Srinivas, J.W. King, L.R. Howard, J.K. Monrad, Solubility and solution thermodynamic properties of quercetin and quercetin dihydrate in subcritical water, J. Food Eng. 100 (2010) 208–218, https://doi.org/10.1016/j.jfoodeng.2010.04.001.

[57] G.S. Borghetti, J.P. Carini, S.B. Honorato, A.P. Ayala, J.C.F. Moreira, V.L. Bassani, Physicochemical properties and thermal stability of quercetin hydrates in the solid state, Thermochim. Acta 539 (2012) 109–114, https://doi.org/10.1016/j.tca.2012.04.015.

[58] R. Bogel-Łukasik, L.M. Nobre Gonçalves, E. Bogel-Łukasik, Phase equilibrium phenomena in solutions involving tannins, flavonoids and ionic liquids, Green. Chem. 12 (2010) 1947–1953, https://doi.org/10.1039/c0gc00308e.

[59] L. Chebil, C. Humeau, J. Anthony, F. Dehez, J.M. Engasser, M. Ghoul, Solubility of flavonoids in organic solvents, J. Chem. Eng. Data 52 (2007) 1552–1556, https://doi.org/10.1021/je7001094.

[60] S.S. Amer, W. Mamdouh, M. Nasr, A. ElShaer, E. Polycarpou, R.T.A. Abdel-Aziz, O. A. Sammour, Quercetin loaded cosm-nutraceutical electrospun composite nanofibers for acne alleviation: preparation, characterization and experimental clinical appraisal, Int. J. Pharm. 612 (2022), https://doi.org/10.1016/j.ijpharm.2021.121309.

[61] K.P.S. Hussan, G. Govindaraj, T. Correia, N. Shinyashiki, M.S. Thayyil, T.D. Babu, Molecular dynamics and interactions in amorphous solid dispersion of Erlotinib HCl for improved cancer therapy, Mol. Struct. 1336 (2025), https://doi.org/10.1016/j.molstruc.2025.142014.

[62] B. Dielectric, Dielectric Modulus: Experiment, Application, and Interpretation, (n. d.) http://the-dielectric-society.org/sites/default/files/richert2005.pdf.

[63] E. Pereira, Data Analysis with the Vogel - Fulcher - Tammann - Hesse Equation, J. Phys. Chem. A 108 (2004) 10824–10833.

[64] H. Vogel, The Temperature Dependence Law of the Viscosity of Fluids, Phys. Z. 22 (1921) 645–646.

[65] C.A. Angell, R.D. Bressel, J.L. Green, H. Kanno, M. Ogunill, E.J. Sare, Liquid Fragility and the Glass Transition in Water and Aqueous Solutions 22 (1994) 115–142.

[66] L.M. Wang, C.A. Angell, R. Richert, Fragility and thermodynamics in nonpolymeric glass-forming liquids, J. Chem. Phys. 125 (2006) 1–8, https://doi.org/10.1063/1.2244551.